Study of the Mutual Interaction between a Wing Wake and an Encountering Airplane

by

A. B. Walden
C. P. van Dam

Department of Mechanical and Aeronautical Engineering
University of California
Davis, CA 95616

NASA Grant No. NAG1-1572
Final Report

March 1996

Abstract

In an effort to increase airport productivity, several wind-tunnel and flight-test programs are currently underway to determine safe reductions in separation standards between aircraft. These programs are designed to study numerous concepts from the characteristics and detection of wake vortices to the wake-vortex encounter phenomenon. As part of this latter effort, computational tools are being developed and utilized as a means of modeling and verifying wake-vortex hazard encounters. The objective of this study is to assess the ability of PMARC, a low-order potential-flow panel method, to predict the forces and moments imposed on a following business-jet configuration by a vortex interaction. Other issues addressed include the investigation of several wake models and their ability to predict wake shape and trajectory, the validity of the velocity field imposed on the following configuration, modeling techniques and the effect of the high-lift system and the empennage. Comparisons with wind-tunnel data reveal that PMARC predicts the characteristics for the clean wing-body following configuration fairly well. Non-linear effects produced by the addition of the high-lift system and empennage, however, are not so well predicted.

Table of Contents

List of Figures

List of Tables

Nomenclature

Symbols

α	Angle of attack
α_o	Angle of attack at zero lift
δ_f	Flap deflection angle
ΔZ	Vertical distance between vortex core and C.G. of following configuration
ΔY	Horizontal distance between vortex core and C.G. of following configuration
Φ	Velocity potential
φ	Perturbation potential
Λ	Sweep angle
μ	Doublet strength
ρ	Density
σ	Source strength
ω	Under-relaxing factor
AR	Aspect ratio
b	Wing span
$\bar{c}$	Mean aerodynamic chord
C_L	Total lift coefficient
C_{L_α}	Total lift-curve slope
C_l	Rolling moment coefficient
C_m	Pitching moment coefficient
C_{m_α}	Pitch-curve slope
C_{m_o}	Pitching moment coefficient at zero lift
C_n	Yawing moment coefficient
c_r	Wing root chord
c_t	Wing tip chord
C_Y	Side force coefficient
E	Jones edge-velocity factor
q_∞	Dynamic pressure
Re	Reynolds Number
$\bar{r}$	Wake shape vector, Point vector to surface panel (appendix)
S	Reference wing area
t/c	Airfoil thickness ratio
U_∞	Freestream velocity
$\bar{V}$	Velocity Vector
v	Sidewash velocity
w	Upwash velocity
x/b	Non-dimensional downstream distance from quarter chord of generating wing

Subscripts

b	body
body	body axes
f	following model
g	generating wing
new	new wake geometry
PMARC	PMARC axes
w	wake
wind	wind axes

Acronyms

CFD	Computational Fluid Dynamics
FAA	Federal Aviation Administration
IFR	Instrumental Flight Rules
IMS	Instrument Meteorological Conditions
NASA	National Aeronautics and Space Administration
NLR	Nationaal Lucht - En Ruimtevaartlaboratorium - National Aerospace Laboratory of the Netherlands
PMARC	Panel Method Ames Research Center
TAP	Terminal Area Productivity
VFR	Visual Flight Rules
2-D	Two-Dimensional
3-D	Three-Dimensional

1.0 Introduction

The need to increase the capacity of the National Airspace System and to decrease delays at airports has caused a renewed interest in wake-vortex research. A variety of runway traffic capacity simulations have been performed on several high-traffic volume airports with distinct runway configurations: single runway, independent parallel runways, closely spaced dependent runways, and intersecting runways.[1,2,3] These studies show that a decrease in separation standards between aircraft not only results in significant reductions in delay time, saving airlines millions of dollars in operating costs per year, but also creates increases in revenue attributable to the increase in air traffic capacity.[1] Reducing separation standards can therefore be very beneficial to the economy as well as the aviation industry.

	Leading Aircraft		
Following Aircraft	Heavy (>300k lb)	Large (<300k ,>12.5k lb)	Small (< 12.5k lb)
Heavy	4 / 2.7*	3 / 1.9*	3 / 1.9*
Large	5 / 3.6*	3 / 1.9*	3 / 1.9*
Small	6 / 4.5*	4 / 2.7*	3 / 1.9*

* VFR values: These are based on measured spacings not standard regulations.[1]

Table 1.1 Current U.S. IFR and VFR Separation Spacings (Nautical Miles)

Current separation spacings are shown in Table 1.1 for both VFR (Visual Flight Rules) and IFR (Instrumental Flight Rules) flight conditions.[1,4] However, these current U.S. separation standards are based on vortex encounter flight tests carried out under "worst case" conditions.[5] With the current emphasis on increasing capacity, it is appropriate to reevaluate current separation standards and determine if they can be safely reduced. NASA, in conjunction with the FAA, is currently conducting research directed at finding ways to safely reduce

the spacing between aircraft in the terminal area through the terminal area productivity (TAP) program.[6,7] TAP's main goal is to achieve fair weather (VFR) airport capacity in instrument meteorological conditions (IMC) through four elements: Air Traffic Management, Aircraft-Air Traffic Control Systems Integration, Low-Visibility Landing and Surface Operations, and Reduced Spacing Operations. It is under the Reduced Spacing Operations element that the present research is based.

Efforts to increase airport capacity include the alleviation of wake hazard by changing the aerodynamic characteristics of the leading aircraft[8,9] as well as utilizing wake detection systems such as Doppler Global Velocimetry[10] or airborne aerodynamic sensors[11]. To date, however, no practical solutions have been obtained for vortex alleviation, and research is still being conducted to obtain more sensitive vortex detection systems. Safety concerns limit the feasibility of conducting flight research on spacing criteria near the ground, therefore greater emphasis on the development, validation, and use of mathematical models for determining minimum safe spacings is an important aspect of the program.

There have been several mathematical models and computational methods developed to study and analyze the wake-vortex interaction phenomenon. Two-dimensional wake roll-up studies have been done by Krasny[12] and Moore[13]. However, 2-D calculations suffer many limitations if wakes of real aircraft are to be computed. The effects of sweep, taper, downwash, and finite-wing effects are not taken into account. Additionally, 2-D codes fail to account for the interaction between the wake and a 3-D aircraft configuration which includes a fuselage, empennage, and nacelles. 3-D roll-up calculations were later completed by Butter and Hancock[14] using a point-vortex method, Yeh and Plotkin[15] using a higher-order panel method,

and Ribeiro and Kroo[16], utilizing the vortex-lattice method coupled with the vortex-in-cell method. An excellent survey of numerical methods for vortex-flow simulations is given by Hoeijmakers[17].

Recently, some of these analyses have been extended to the wake-vortex interaction problem. The most complete method to employ would be numerical calculations based on the Navier-Stokes equations or the Euler equations. The advantage of these methods is that regions with vorticity are "captured" rather than "fitted" as in the case of methods based on the potential-flow equations. Therefore viscous effects, shock waves, and the convection of rotational flow can be captured. These methods, however, are computationally demanding both in CPU time and computer memory and often require many man-hours to produce the computational grid. Furthermore, solutions generated by these methods tend to be affected by numerical dissipation. Kandil, Wong, and Liu[18] solved for the flow-field interaction between a tip vortex generated by a Boeing 747 wing, and a following Boeing 747 wing through the use of the Reynolds-averaged Navier-Stokes equations. The rolling moment of the following configuration is subsequently obtained from the dynamics equation of rolling motion. The addition of a fuselage, empennage, and flaps to the computational model, however, would greatly increase the complexity of the problem and result in a substantial increase in both man hours required for flow-field grid development and in the computational time required for solutions to be obtained.

The vortex-lattice method is the most widely used method. Examples of this type of modeling are presented by Behr and Wagner[19], Bloy and West[20], and Rossow[21]. Vortex-lattice theory is based on the representation of a lifting surface by a lattice of vortex filaments. These filaments or line vortices trail

downstream forming horse-shoe vortices. The objective is to solve for the vorticity distribution over the lifting surface such that the bound and trailing vortices will cancel all freestream velocity components normal to the surface. The Kutta condition, which specifies a zero-pressure jump in the flow at the trailing edge of the lifting surface, also has to be satisfied. The vortex-lattice method is more accurate for thin wings having little camber than for thick wings with a high degree of camber, because the lifting surface is represented by a planar surface. This method tends to produce good results when the encountering configuration is much smaller than the configuration that generates the vortex system (i.e. the generator), but its accuracy rapidly diminishes when the encountering configuration is of equal or greater size than the generator. What is typically neglected in these studies is that at subsonic flight conditions the flow field of the encountering airplane can have a significant effect on the vortical flow field of the generating configuration particularly when both encountering aircraft have approximately the same size and mass. Stewart[22] shows that the interaction effects can be significant and can reduce the calculated roll angle in the first second of the encounter by 20%.

Another popular method which utilizes the potential-flow equations is the panel method. Three-dimensional panel methods have an advantage over vortex-lattice methods in that thickness and camber effects are included resulting in a more accurate configuration representation. Furthermore, non-linear effects such as wake roll-up and the effects of boundary-layer growth on the solutions can be modeled. These codes are often more beneficial than field methods because of their ability to model complex configurations without the necessity of generating complex flow-field grids. Grid discretization is required merely for the surface of the 3-D configuration. Smith and Ross[23] compare experimental lift and rolling moments with the

computational results obtained from the panel method VSAERO[24] for a wake vortex/wing interaction. Good agreement was obtained with experimental data when the following wing was located more than one following-wing chord length from the tip vortex. However, the code consistently overestimated the induced rolling moments at large distances downstream. A more precise estimation of the aerodynamic characteristics can be attained by modeling the entire following configuration and including the interactions with the wake. Furthermore, the inclusion of the fuselage and empennage allows the prediction of pitching and yawing moments as well as rolling moments.

The purpose of this study is to investigate the ability of a low-order panel method code, PMARC (Panel Method Ames Research Center), to predict the longitudinal and lateral-directional characteristics of a following aircraft configuration at varying distances from a vortex-generating wing. Unlike previous studies, the entire following configuration including the fuselage, empennage, and flaps is modeled. Following this introduction, a brief description of the code and its related features will be presented along with a test case to validate the code for this type of study. A description of the wind-tunnel experiment used for the validation of the computational results will then be given. This will be followed by a description of the computational models used for the generating configuration, the following configuration and the trailing vortex systems. Comparisons with the experimental results obtained in the wind-tunnel will then be discussed. Finally, several conclusions and recommendations will be presented.

2.0 Computational Method and Theory

Panel methods have been widely used in a variety of applications from the study of flows about complex aircraft configurations to the analysis of flows around propellers, automobiles, shiphulls, sails, and submarines. Several panel methods have been developed and are currently in use in industry, some of which are described in reference 25. These panel methods can be divided up into two categories: low-order panel methods in which the singularities are distributed with constant strength over each panel, and higher-order panel methods in which the singularity strengths are allowed to vary linearly or quadratically over each panel. Higher-order panel methods claim better accuracy in modeling the flow field but at a higher computational expense. However, new generation low-order panel methods have proven to obtain the same level of accuracy as higher-order panel methods with a substantial reduction in computing time.[26]

2.1 Description of PMARC

PMARC is a new generation low-order panel method code with the capability of predicting incompressible, inviscid flow fields around complex three-dimensional geometries.[27,28] The code was written as an open code allowing other government agencies and contractors to make contributions and modifications. Furthermore, the code allows for the arrays to be adjusted permitting the user to run on computers ranging from personal computers to supercomputers. The most current version of this code, Version 12.19, was used for the present study.

Advanced features available in PMARC include internal flow modeling for ducts and wind-tunnel test sections, simple jet-wake modeling, a time-stepping wake model, and an integral boundary-layer routine. The code also has the capability of computing the velocity, Mach number, and pressure

coefficients at arbitrary points in the flow field through rectangular or cylindrical velocity scans. Another capability which was very beneficial to the present study is the ability to trace off-body and on-body streamlines. Streamlines are traced upstream and downstream according to the computed local velocities from a user-specified origin.

Like all panel methods, PMARC is based on several assumptions. First of all, an inviscid and incompressible flow field is assumed. Secondly, it is assumed that there is no flow separation other than at the sharp trailing edges of lifting surfaces. And finally, infinitely thin vortex sheets are used to model the trailing vortex system. The configuration in the potential flow is modeled as a closed body divided into panels. This body is represented by constant-strength source and doublet distributions on each panel. The Dirichlet boundary condition is enforced on the collocation points, or control points, on each panel to allow for the solution of the velocity potential. An explicit solution of the source strengths can be found based on a zero or prescribed normal velocity on the surface. Once these source strengths are known, the doublet strengths can be determined through an integral equation based on the Dirichlet boundary condition being prescribed on the potential flow inside the body. The wake is modeled using doublet panels whose solutions can be obtained by enforcing the Kutta condition on the trailing edges or separation lines of the lifting body. Once the doublet solutions are obtained, the doublets on the surface are numerically differentiated to attain the surface velocity components from which the pressure coefficients and subsequently the force and moment coefficients are obtained. A concise mathematical description of the potential theory on which PMARC is based can be found in Appendix A.

2.2 Code Validation

The ability to represent wake formation is essential in modeling the complex wake-vortex interaction problem. In particular, the wake shape of the generating wing should be correctly predicted in order to accurately locate the core of the wake as well as correctly compute the surrounding velocities at specified distances. The capability of the PMARC code is validated and compared to a test case described by Hoeijmakers[29]. The original calculations were completed by Labrujere and O. de Vries[30] utilizing a potential-method code developed at the National Aerospace Laboratory of the Netherlands or NLR. The configuration consists of a 30° swept-back wing with a constant chord and circular wing tips. The airfoil section is a NACA 0012-64 and is constant along the span. Furthermore, the wing has a linearly distributed twist of 4° rotated about the 50% chord location. Geometric characteristics of this model are depicted in Figure 2.1.

Calculations were performed at two different lift coefficients for the wing, C_L of 0.50 and 0.82. Due to the tunnel-wall constraint as well as viscous effects, the measured lift differed from the lift predicted by the potential code for a given angle of attack. Therefore, since lift is one of the crucial parameters that determine vortex shape and strength, calculations were performed at the same lift coefficient rather than the same angle of attack. PMARC produced identical lift coefficients at the same angle of attack as the NLR method; α=8.7° for a C_L of 0.50 and an α=13.65° for a C_L of 0.82. As expected, these α's were slightly less than the experimental results because of the aforementioned wall constraints affecting the flow field.

2.2.1 Various Wake Configurations

Several wake techniques were used to calculate the wake characteristics. These included a rigid wake, time-stepping wake and a streamline-based wake

technique. The two wake options that PMARC implements are the rigid wake and the time-stepping wake. The rigid wake is aligned with the freestream velocity and contains a constant doublet strength in the streamwise direction. The rigid-wake approximation, containing straight vortex lines, renders the potential problem linear. The rigid wake technique, however, can not predict wake shape. Unlike the rigid wake techniqe, the time-stepping wake technique has the ability to predict wake shape by simulating unsteady aerodynamics. The time-stepping wake is time-stepped with the local velocity from a time t=0. At each subsequent time step, a new row of doublet panels is shed downstream and aligned with the local velocity field creating a realistic wake shape. Another widely used wake technique is the streamline-based wake technique. Like the time-stepping wake technique, the streamline-based wake technique is based on the understanding that the wake lines in a flow are generally aligned with the local velocity field. First, the complete solution for a rigid wake is obtained. An off-body velocity scan is then performed aft of the trailing edge to the end of the wake downstream. Streamlines are then traced from these velocities. These streamlines are subsequently used as the initial wake input and the PMARC code is run again. Since the new wake is aligned with the local velocities, an improved location of the wake surface arises. The best results were obtained when the streamlines were traced right aft of the trailing edge as seen in Figure 2.2. Successive iterations proved fruitless causing the wake to "unroll" and lose its shape. Streamline calculations were also performed with an under-relaxing factor, ω, of 0.5 in hopes of damping and delaying wake formation to improve consecutive iterations. This can easily be seen through the equation:

$$\vec{r}_{new} = \vec{r}_{old} + \omega(\vec{r}_{calculated} - \vec{r}_{old})$$

where $\bar{r}$ represents the wake shape. However, this proved to be ineffectual as well.

2.2.2 Comparisons and Results

PMARC's ability to model wake shape and wake roll-up can clearly be seen in Figures 2.3a and 2.3b. Here, the streamline-based wake shape and the time-stepping wake shape are calculated and compared with experimental and NLR computational results for various distances downstream. Experimental results were obtained through the measurement of the total head loss in the wake with a pitot rake, while numerical results were obtained through a panel method developed at NLR. The streamline-based wake and the time-stepping wake were calculated with the same number of wake stations to keep comparisons consistent with the NLR calculations. In order to perform this comparison, the time-stepping wake was time-stepped a total time of 200 seconds with a time-step of 10 seconds from time t=0. Furthermore, the computed wake length was limited to be approximately 1.6 times the span of the swept wing, equivalent to that of the NLR results. The solution utilizing the streamline-based wake required approximately 40.0 CPU seconds on a CRAY Y-MP, while the solution with the time-stepping wake demands approximately 65.0 CPU seconds.

The present calculations show better agreement with the experimental results than the NLR calculations. At the lower lift coefficient, present results show a much better representation of the experimental wake shape than the NLR calculations as seen in Figure2.3a. At a higher angle of attack, however, both the streamline-based wake and the time-stepping wake show poor agreement with the experimental data in the mid-semi-span region and exhibit nearly the same trends as the NLR computations. The roll-up, however, is still fairly well predicted. The streamline-based wake shows a slightly better

comparison than the time-stepping wake. This is more clearly visible as seen in the downstream wake descent comparison shown in Figure 2.3b. Except near the trailing-edge region for a C_L of 0.82, the streamline-based wake displays a much better characterization of the experimental wake-vortex descent than the time-stepping wake and the NLR calculated wake at both lift coefficients. The improvement, however, is seen to decrease as lift coefficient is increased. These improved results coupled with the shorter time necessary to run the code, indicate that the streamline-based wake technique is the preferred technique to model the wake of the generating wing in the study of the wake-vortex interaction.

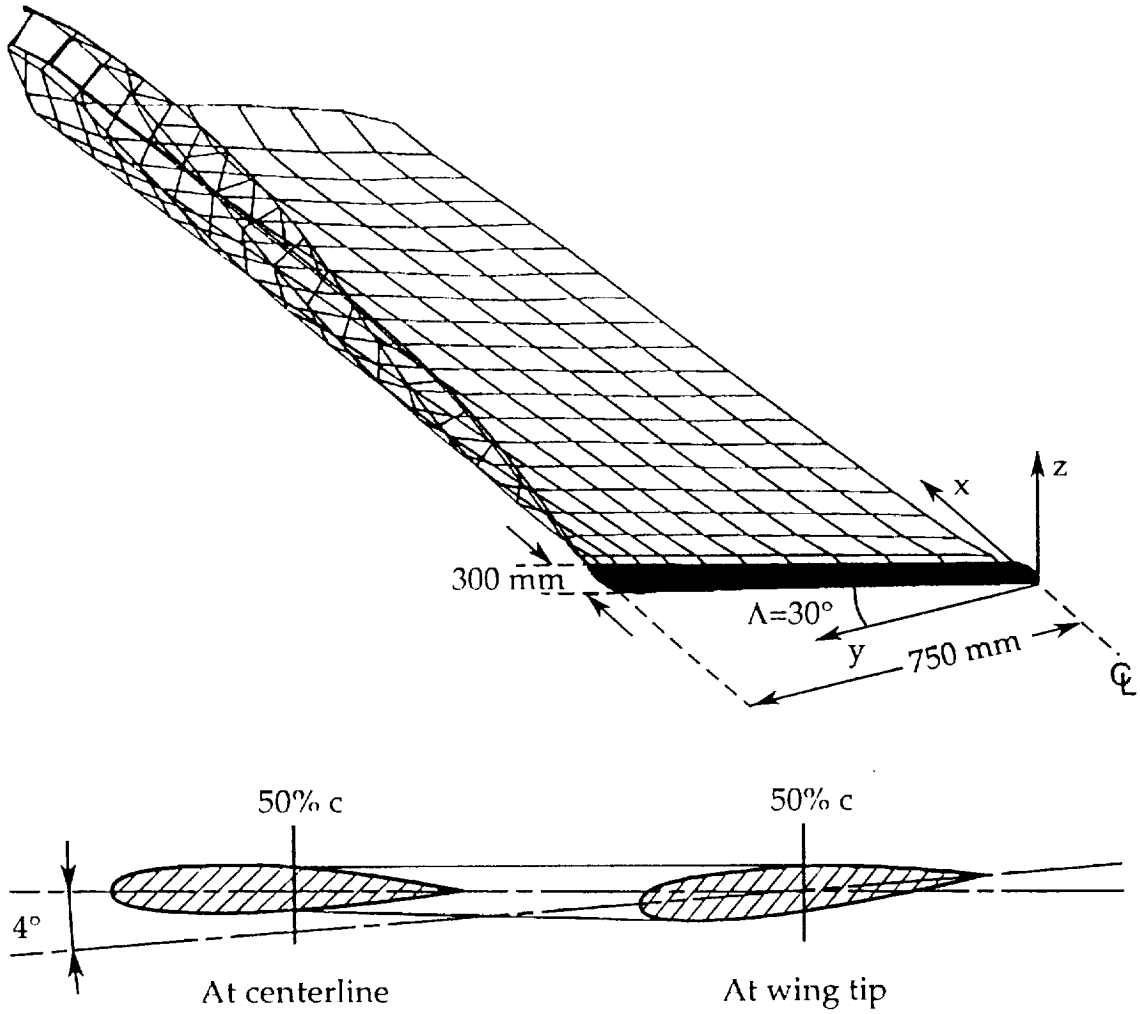

Profile NACA 0012-64

Figure 2.1 Geometric Characteristics of the NLR Test Case With A Time-Stepping Wake

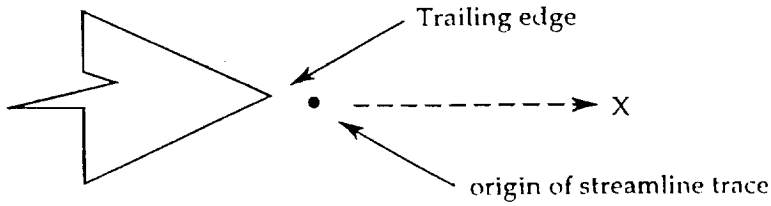

Figure 2.2 Prime Placement of a Streamline Trace

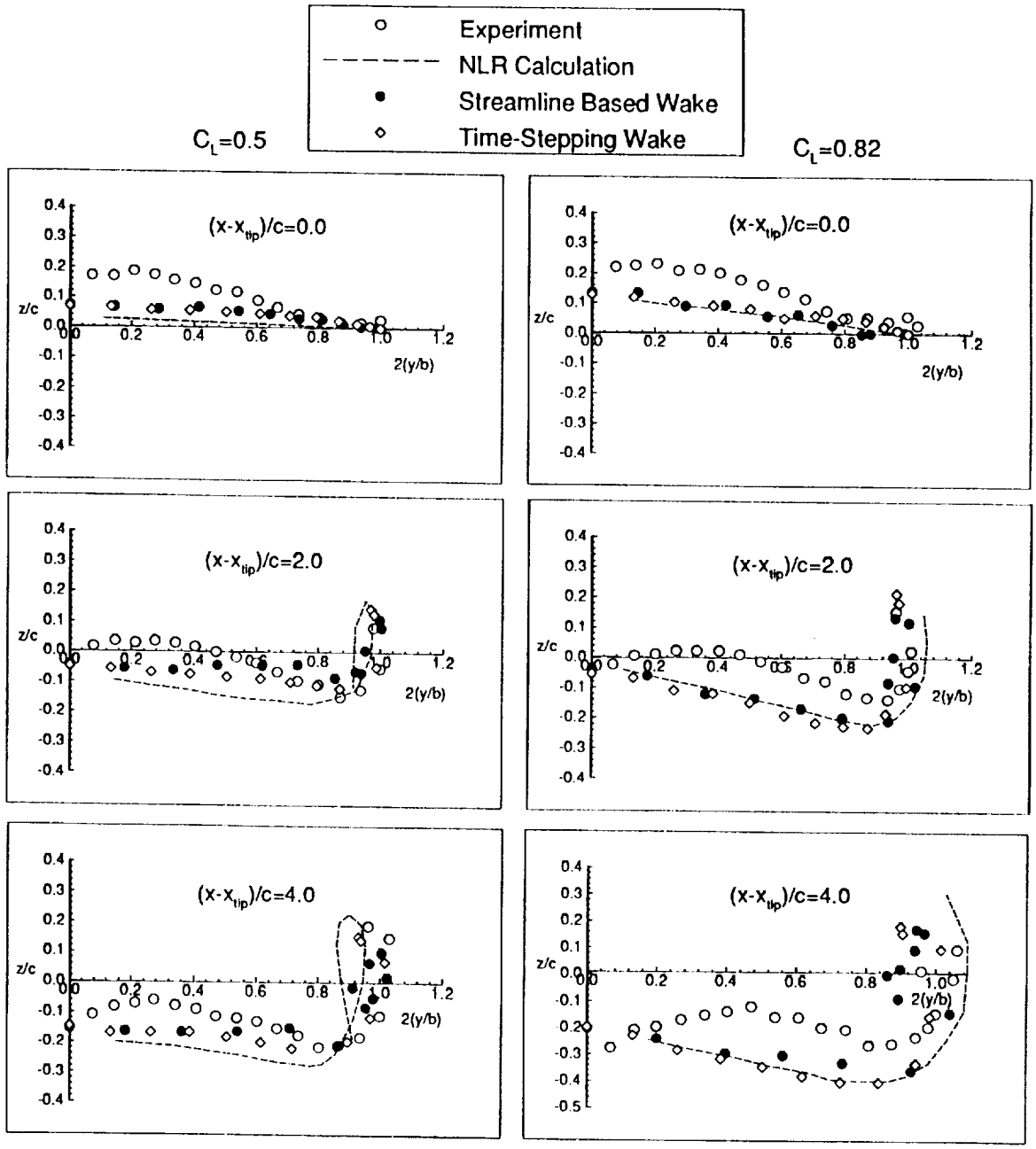

(a)

Figure 2.3 Computed and Measured Wake Vortex Geometry for the NLR Test Case (a) Comparison of Wake Roll-up and Shape

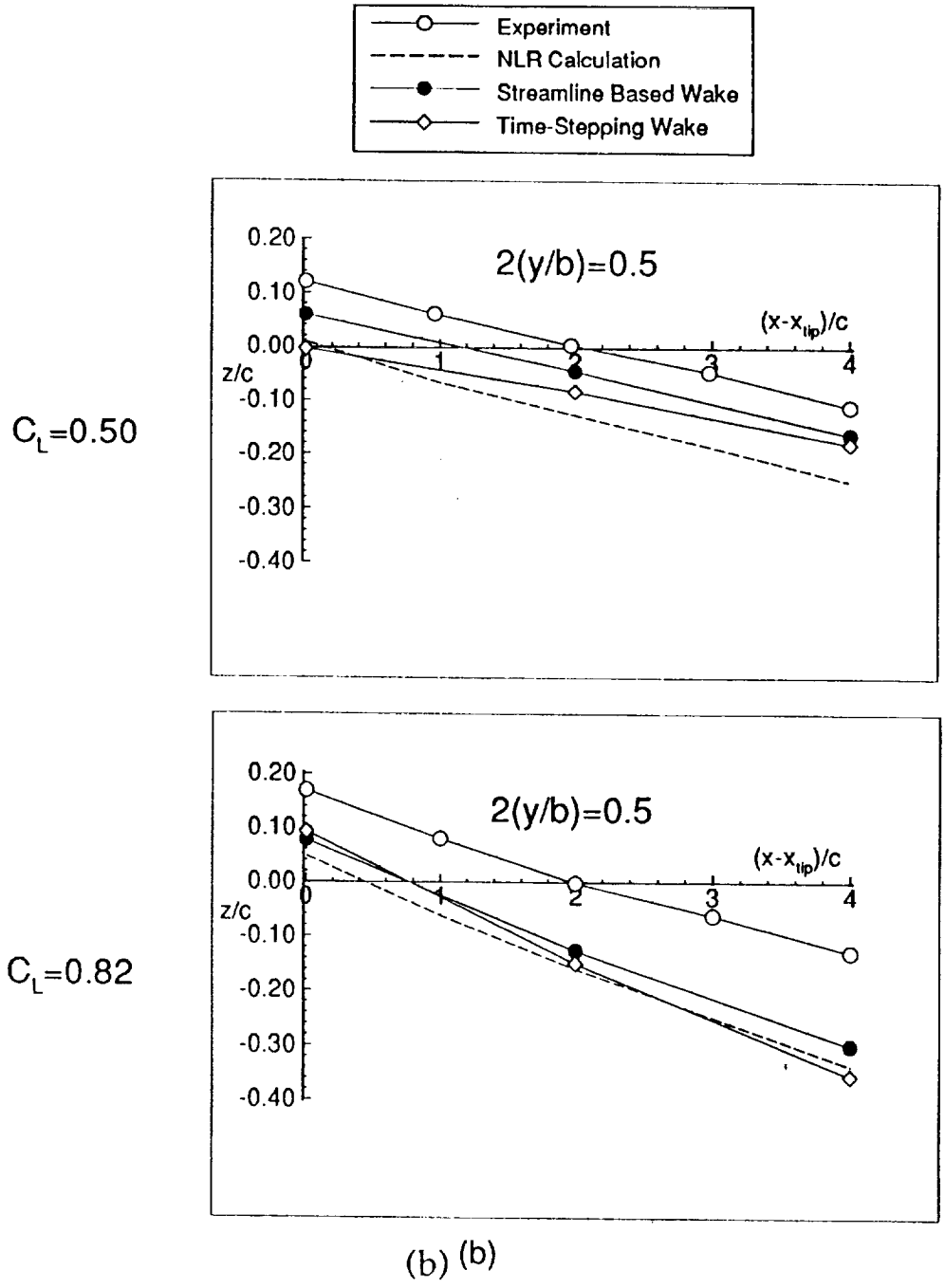

Figure 2.3 Computed and Measured Wake-Vortex Geometry for the NLR Test Case (b) Comparison of Wake Descent

3.0 Description of Wind-Tunnel Experiment

A low-speed wind-tunnel investigation of the wake-vortex interaction was conducted in the NASA Langley 30-by 60-foot tunnel. Static force and moment tests were performed at a dynamic pressure, q_∞, of 9.0 psf corresponding to a freestream velocity, U_∞, of 87 ft/s and a Reynolds number of 0.95×10^6 based on the freestream velocity and the chord length of the generating wing. A 12-foot rectangular planform wing with an NLF(1)-0215F airfoil was used to generate the vortex system. This airfoil was designed for a high-performance, single engine, general-aviation airplane.[31] Tests were limited to two circulation strengths which corresponded to lift coefficients of 0.94 and 1.18. These lift coefficients corresponded to α's of approximately 2.5° and 4.6°. Tubes through which smoke was injected into the vortex flow field were attached along the trailing edge of the generating wing. The tubes, which have a diameter of approximately 0.5 inches, modified the camber of the airfoil, causing a shift in the lift curve. The effect of the tubes on the camber of the airfoil is shown in Figure 3.1. The smoke tubes allowed for the measurement of the distance between the vortex and following aircraft model. Although experimental testing limited the following model's ability to vary its distance with respect to the *left* generating wing vortex only, smoke tubes had to be placed on both sides to prevent asymmetric loading.

The 17.5%-scale model used for the following airplane represented a generic business/commuter aircraft. Coe, Turner, and Owens[32] fully describe the geometric characteristics of this model. Modifications to the model used in the present wind-tunnel test include the removal of the two 5-bladed propeller systems as well as the permanent addition of the full-span Krüger flaps. This model is shown in Figure 3.2. Basic geometric characteristics of both following and generating models are listed in Table 3.1. Because the intent of the

investigation was to explore the high-lift landing-approach condition, the majority of the tests were performed with the trailing-edge flaps of the following model deflected at 35°. Tests were also performed with the horizontal and vertical tails removed, the trailing-edge flaps set to zero, and the Krüger flaps removed. The angle of attack of the following model ranged from -6° to 15°. Sideslip angles ranged from -10° to 10°.

Wing Parameters	Generating Wing	Following Model
AR	7.0	8.3
b	12 ft	9.072 ft
$\bar{c}$	1.714 ft	1.181 ft
S	20.568 ft^2	9.869 ft^2

Table 3.1. Basic Geometric Wing Characteristics For Both Models

Measurements were taken at a downstream distance of 2.02 times the span of the generating wing. This distance was measured from the quarter chord of the generating wing to the center of gravity of the following aircraft. The spanwise (horizontal) and vertical distances between the center of gravity of the following aircraft and the vortex core created by the generating wing were varied. These distances were, ±20, ±40, and ±60 inches for the horizontal distance, ΔY, and ±20, ±40, -48.4, and +60 inches for the vertical distance, ΔZ. These distances were varied such that the generating wing traversed while the following business/commuter model was fixed. Figure 3.3 depicts the associated sign conventions used during the wind-tunnel experiment. A photograph of the test set-up in the wind-tunnel is shown in Figure 3.4.

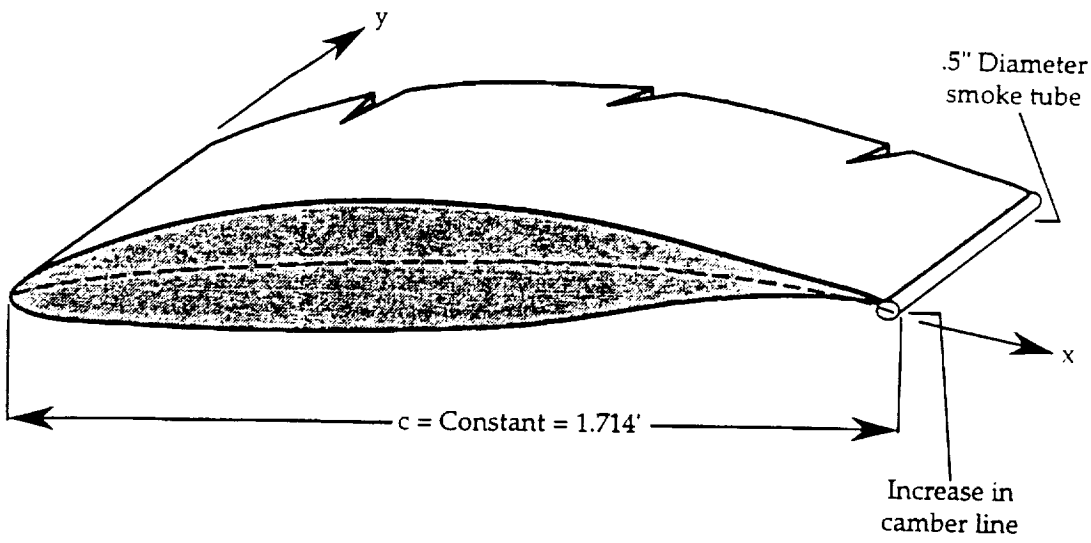

Figure 3.1 Cross-Section of the Generating Wing Model With Associated Smoke Tubes

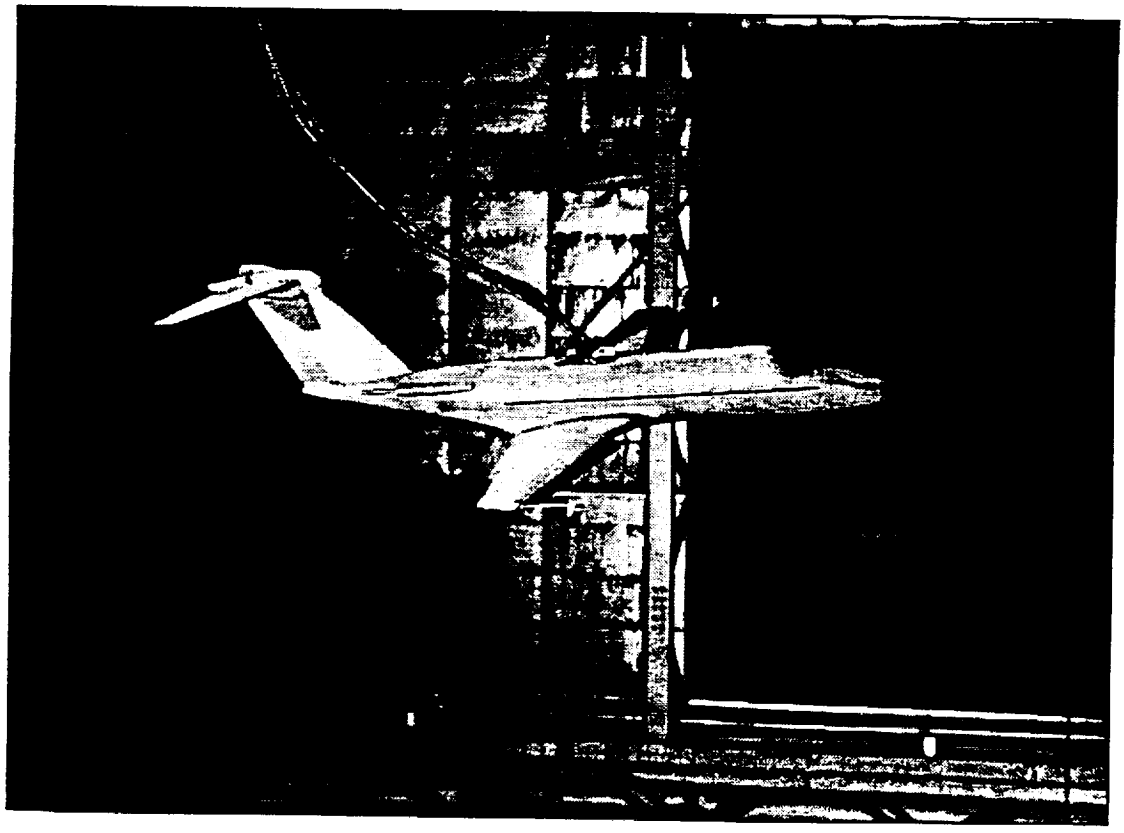

Figure 3.2 Following Generic Business Jet Pictured Here During a Free-Flight Test

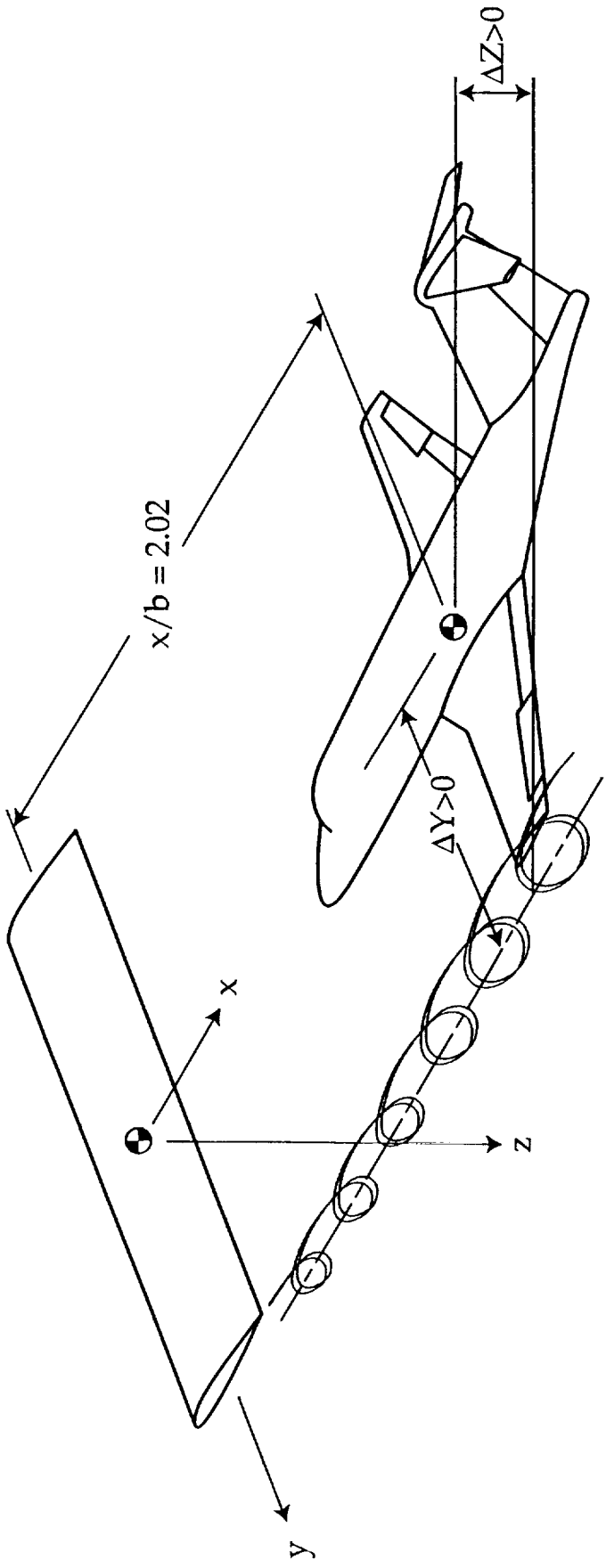

Figure 3.3 Axes System and Sign Convention Used in Experiment

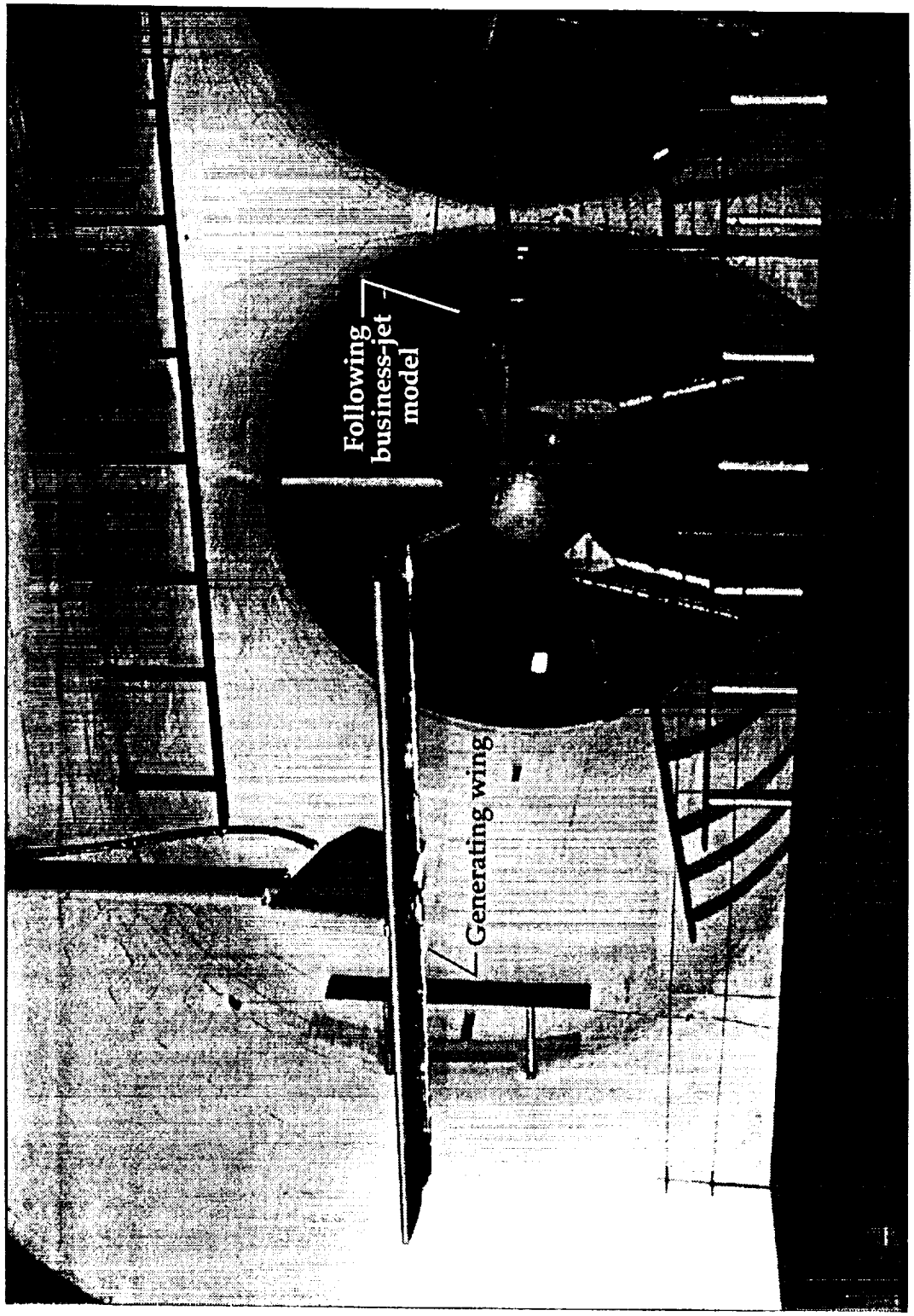

Figure 3.4 Set-Up of the Vortex Interaction Experiment in the 30x60 foot Wind Tunnel

4.0 Modeling the Interaction

The panel method has an advantage over most CFD methods in that it requires only surface-grid generation rather than a very time-consuming grid generation for the entire flow field. However, creating the surface grid is still an involved procedure. The geometry of the entire wake-vortex interaction problem is defined in a body-fixed, global coordinate system. Separate coordinate systems are designated for each configuration, i.e. the generating wing and the following aircraft. The surface of each configuration is subdivided into a number of surface "patches" or curved surfaces which are further divided into quadrilateral "panels". The number of panels is indicative of the size of the problem that has to be solved since the body is modeled by constant-strength source and doublet distributions over each panel. Care is taken such that the normal of each surface panel points outward into the flow field of interest. At least two sections are used to define a surface patch. These sections consist of several points which define a certain curvature at a specific juncture in the geometry.

4.1 Geometry

In most aerodynamic-flow problems, only half of the surface geometry requires modeling since a symmetrical flow field and configuration can be assumed. The wake-vortex interaction problem, however, can produce asymmetrical flow fields on both the generating wing and the following model. Therefore, both configurations had to be completely modeled. The distance between the generating wing and the following model as well as the dimensions of both modelss were normalized with respect to the span of the generating wing.

4.1.1 Generating Wing Model

The 12-foot generating wing consisted of a constant chord NLF(1)-0215F section airfoil.[33] In the computational model, panel density and spacing were varied in both the chordwise direction and the spanwise direction to ensure a converged solution with the least amount of panels. The generating wing was modeled using a total of 920 panels, with 20 spanwise stations and 40 chordwise stations. A total of 120 panels were allocated for the wing tips. A spanwise cosine-spacing distribution was chosen to capture the steep pressure gradients near the wing tips. For the same reasons, a half-cosine distribution was chosen for the chordwise direction with a greater panel density near the leading edge. The generating wing model is depicted in Figure 4.1.

4.1.2 Following Business-Jet Model

To ensure the accuracy of the following aircraft model as well as to allow comparisons with the experimental data for various aircraft configurations, the following business jet was modeled in four stages: (1) the wing-only configuration (2) the wing-body configuration (3) the wing-body plus the high-lift devices such as the trailing-edge flaps and the Krüger flaps, and (4) the entire configuration including the empennage. Panel density studies were also performed for the following aircraft configuration to determine the minimum number of panels required to accurately represent the surface geometry and obtain a converged solution. The wing of the following model consisted of a NACA 23015 cross section at the exposed root which tapered linearly down to a NACA 23012 at the tip. A break in the leading-edge sweep of the wing was located at approximately 20% of the semi-span from the exposed root. A half-cosine distribution was chosen for the panel spacing between the root chord and the break chord, while a full-cosine distribution was used between the break chord and the tip chord. These spacings were chosen to allow for a

greater panel density near the break chord to capture the changes in the pressure distributions in this region.

The wing-only model consisted of a total of 1480 panels, with 40 chordwise stations and 17 semi-span wing stations. A total of 120 panels were allocated for the wing tips. In place of the fuselage, the wing-only model utilized a NACA 23015 airfoil to generate the lifting surface from the exposed root chord to the actual root chord. The leading-edge and trailing-edge sweep angles were kept constant at this section to insure continuity. The surface geometry of the following wing-only model is pictured in Figure 4.2.

The computational configurations including the fuselage and the high-lift system are shown in Figure 4.3 and Figure 4.4. The addition of the fuselage resulted in a total of 2856 panels. The implementation of the high-lift system required an increase in the spanwise paneling density of the wing. The addition of the trailing-edge flaps and the full-span Krüger flaps resulted in a surface geometry consisting of 5664 panels. Both trailing-edge flaps were modeled as wings with an increase in panel density near the leading edges. These flaps were deflected at 35°. The Krüger flaps extended from the wing break to the tip and was modeled with varying curvature as defined by Coe et al. (reference 32).

The high-lift system on the wind-tunnel model, however, had very complex geometries associated with it including brackets to attach the high-lift system to the main element. Furthermore, the cove on the main element which is used to store the retracted trailing-edge flaps, is comprised of sharp edges. Inviscid methods tend to have difficulty obtaining accurate solutions near regions with sharp discontinuities due to their inability to capture regions of vortical flow due to viscous effects. These sharp coves were replaced by a smoother streamlined geometry to approximate the shape that the inviscid

flow experiences in the coves. Like the trailing-edge flap coves, the Krüger-flap coves were also modified in a similar manner to more accurately model the inviscid-flow behavior as well as to improve solution convergence. Note that the brackets were not modeled for further simplicity. At first, due to it's relatively "thin" geometry, the Krüger flaps were modeled with "zero"-thickness panels that were implemented with the Neumann boundary condition instead of the Dirichlet boundary condition. It was discovered that by imposing the Dirichlet boundary condition on the Krüger flap panels, the required CPU time was significantly reduced[34], while attaining the same overall results. To implement the Dirichlet boundary condition, the Krüger flaps were modeled with some degree of thickness while still maintaining the streamlined cove shape. The CPU time was not only cut in half, but the number of iterations required to obtain a converged solution decreased by almost three-fold. The differences between the computational geometry and the actual geometry are illustrated in Figure 4.5.

The full-computational configuration is shown in Figure 4.6. The horizontal and vertical tails were modeled as the wing, in that the panel density was increased towards the leading edge to capture the steep pressure gradients in this area. A cosine spacing in the spanwise direction was utilized for the horizontal tails. The addition of the empennage required an increase in fuselage paneling resulting in a final surface geometry consisting of 7098 panels.

4.1.3 Comparison with Experimental Data

Before an analysis of the wake-vortex encounter could be performed, the experimental characteristics of both the generating wing and the following business jet model had to be compared individually with the computational results. The wake of the generating wing was modeled using both the rigid

wake technique and the streamline-based wake technique. The rigid wake technique was selected to simulate steady-state conditions, while the streamline-based wake technique was selected for its ability to predict wake shape and roll-up as well as its low CPU memory requirement in contrast with the time-stepping wake technique. Due to memory requirements and time limitations, only the rigid wake technique was used for the following configuration.

The experimental and calculated lift curves for the generating wing are shown in Figure 4.7. The addition of the smoke tubes which were placed on the trailing edge of the generating wing had a significant effect on the experimental results. Due to the complexity of modeling the surface geometry of the smoke tubes, the generating wing was not modeled with the smoke tubes. Because of this modeling discrepancy as well as the viscous effects in the wind-tunnel experiment, the measured lift differed from the lift predicted by the present calculation. To account for these discrepancies in lift coefficient, calculations were performed at the same lift coefficient rather than the same angle of attack. It can readily be seen in Figure 4.7 that the streamline-based wake technique produces a slightly lower lift-curve slope than the rigid wake technique. Moreover, since PMARC is based on inviscid theory, it can not predict the stalling effects as those observed in the experimental data. Table 4.1 displays the angles of attack associated with the experiment and the two wake techniques for a C_L of 0.94 and a C_L of 1.18. As mentioned previously, these were the two lift coefficients used in the wind-tunnel experiment to generate the trailing vortex system.

	C_L=0.94 Angle of Attack:	C_L=1.18 Angle of Attack:
Experimental	2.50°	4.70°
Rigid Wake	5.55°	8.58°
Streamline-based Wake	6.17°	9.35°

Table 4.1 Angle of Attack Associated with Wind-Tunnel Experiment and Two Wake Techniques for the Generating Wing

PMARC's ability to predict lift coefficient is demonstrated in Figure 4.8. Here, the rigid wake solution and the experimental data without the smoke tubes are compared with the 3-D lift-curve slope calculated from the 2-D lift-curve slope which was obtained from previous experimental results for the NLF(1)-0215F airfoil.[33] The 3-D lift-curve slope was calculated using the equation based on lifting-line theory[35]:

$$C_{L_{\alpha(3-D)}} = f \times \left(\frac{C_{L_{\alpha(2-D)}}}{1 + \frac{57.3 \times C_{L_{\alpha(2-D)}}}{\pi \times AR}} \right) \times \left(\cos \Lambda_{c/4} \right)^{\frac{1}{2}} \qquad (4.1)$$

where

$$f = f(AR, c_t/c_r)$$

The present computation is seen to agree with results from lifting-line theory. The wind-tunnel results, however, show a discrepancy at lower angles of attack. In particular, the angle of attack at zero lift (α_o) has a discrepancy of approximately 2° which may be due to strut mount interference. Overall, PMARC results compare well to the wind-tunnel data (without the smoke tubes) within the range required to generate the trailing vortex system.

Unlike the generating wing, the following business jet model utilizes airfoils that are more sensitive to Reynolds number. Figure 4.9 depicts this

sensitivity as it compares the C_L of the following wing-body configuration for various Reynolds numbers. Three curves were obtained for three different Reynolds numbers using three different models: the present wind-tunnel 17.5% scale model (Re=0.6535 million), a 22% scale version of the same model (Re=1.952 million)[36], and the present computational solution (Re= ∞, inviscid solution). The lift-curve slope, C_{L_α}, is shown to increase with an increase in Reynolds number. Calculations of Reynolds number effects were performed using Equation 4.1 in conjunction with 2-D C_{L_α} values obtained from Riegels[37]. Table 4.2 compares these calculated results with experimental results. Riegels' tabulated results reveal a 2-D C_{L_α} dependency on Reynolds number for both the NACA 23015 and the NACA 23012. The calculated 3-D C_{L_α} values are seen to be slightly less than those obtained in the present study. These discrepancies are likely due to a number of reasons including surface roughness effects, airfoil thickness distribution modeling, availability of data and limitations of lifting-line theory. Surface roughness effects were not taken into account in Riegels' 2-D data. Furthermore, the airfoil thickness distribution did not accurately represent the following wing-body configuration. Due to lack of data for various NACA 230 series airfoils, the calculations utilized only NACA 23015 parameters instead of an average of the parameters for the various airfoils across the span. Furthermore, 2-D Riegels data did not account for the fuselage. Another reason for the discrepancy in C_{L_α} could be due to the slight difference in the reference Reynolds numbers used in the calculation (Table 4.2). Finally, discrepancies could have been caused by the limitations of lifting-line theory. Although the finite span of the wing is taken into account in Prandtl's lifting-line theory, the lift and hence the chord are assumed to be concentrated along a single bound vortex. Jones[38] corrects for this chord effect by comparing the potential flow between an elliptic finite plate and an infinite

plate. The edge velocity of the finite plate is seen to be 1/E times that of the infinite plate, where E is referred to as the Jones edge-velocity factor which is defined as the ratio of the semiperimeter of the wing to the span of the wing.[39] Equation 4.1 can therefore be corrected by dividing the 2-D C_{L_α} by E.[39] This would effectively increase the calculated 3-D C_{L_α}. As a whole, Table 4.2 proves the dependency of C_{L_α} on Reynolds number for the following business-jet model.

Actual Re Used In Figure 4.9 Re	Re Corresponding To Riegels' 2-D Airfoil DataUsed in Calculations Re	Actual Slope Obtained In Figure 4.9 C_{L_α}	Calculation (Based on Eqn.4.1 and Riegels' data) C_{L_α}
0.6535 x10^6	0.70 x10^6	.0808 (exp.)	.0771
1.952 x10^6	2.00 x10^6	.0846 (exp.)	.0821
∞	-------	.0928 (PMARC)	-------

Table 4.2 Experimental and Calculated C_{L_α} as a Function of Reynolds No.

Another discrepancy in Figure 4.9 is the value of α_o for all three lift curves. According to Riegels[37] and Abbott and Von Doenhoff[39], α_o is independent of Reynolds number and thickness ratio, t/c, for the NACA 230 series. This value is shown to be approximately -1.2°. Taking the wing incidence angle of 3.18° into consideration, the resulting value for α_o becomes -4.38°. The current wind-tunnel experiment, however, shows an α_o of -2.6°. This discrepancy is currently under further investigation. Also note that like the generating wing, PMARC was unable to model the stalling effects for the following configuration due to its inability to model second-order effects such as separation and viscosity. PMARC is consequently not valid at high angles of attack.

The experimental and computational pitching-moment coefficient comparison is shown in Figure 4.10. It was necessary to shift the calculated moment center 0.72 inches aft from the moment center reference used for the wind-tunnel data to obtain improved results for C_m. The calculated pitch-curve slope, C_{m_α}, is seen to closely match the experimental C_{m_α} once the moment center was altered. Furthermore, C_{m_o} as well as the aerodynamic center is seen to be well predicted as a result of this slight modification.

4.2 Wake Modeling

To ensure the accuracy of the solutions obtained from the wake-vortex interaction modeling, wake studies were performed for both configurations during the vortex interaction with the following wing-only configuration. Wake length was varied for both the following wing-only configuration and the generating wing until the overall aerodynamic results for both configurations did not change. Convergence was achieved when the generating wing had a wake length of at least x/b=7.0 and the following configuration had a wake length of at least x/b=5.0, where b is the span of the generating wing.

4.2.1 Velocity Comparisons

In order to assess the validity of the code in predicting the forces and moments on the following model, the velocities produced by the computed wake of the generating wing were compared to the velocities measured in the wind-tunnel experiment. These experimental velocities were measured by a five-hole probe. Probe measurements were taken at a downstream distance of approximately x/b of 1.28 with a 19 in. x 19 in. grid matrix with points one inch apart. Data obtained from the probe were averages taken during a 20 second time span. An off-body velocity scan was performed for both the rigid wake

and the streamline-based wake to obtain the velocity vectors at the corresponding downstream distance. The generating wing with the streamline-based wake is shown in Figure 4.11. Figure 4.12 shows the streamline-based wake velocity vectors of the generating wing for a C_L of 0.94. Figures 4.13 and 4.14 compare rigid wake and streamline-based wake velocities to experimental upwash and sidewash velocities as a function of ΔZ and ΔY, where ΔZ and ΔY are measured vertical and horizontal distances from the core of the vortex. It can readily be seen that the rigid wake calculation consistently overestimates the velocities near the core. The streamline-based wake calculation is seen to correctly predict the trends of the experimental upwash/downwash and sidewash velocity fields of the wake. Slight discrepancies, however, can be seen near the vicinity of the core. These discrepancies are mainly due to the inability of the code to model viscous effects which are prevalent in the core of the vortex. In addition, vortex core "bursting" and wake dissipation are not taken into account. Another factor that could have contributed to the inconsistency is the observed ±5 in. random movement of the vortex core in the wind-tunnel experiment.

In general, the streamline-based wake exhibits an excellent correlation of the vortex velocities near the core. Although the rigid wake calculations show a slightly higher upwash velocity in the vertical direction, generally good correlation was obtained outside of the core. In conclusion, these correlations demonstrate that both wake techniques are valid techniques in predicting the perturbation velocities outside of the core.

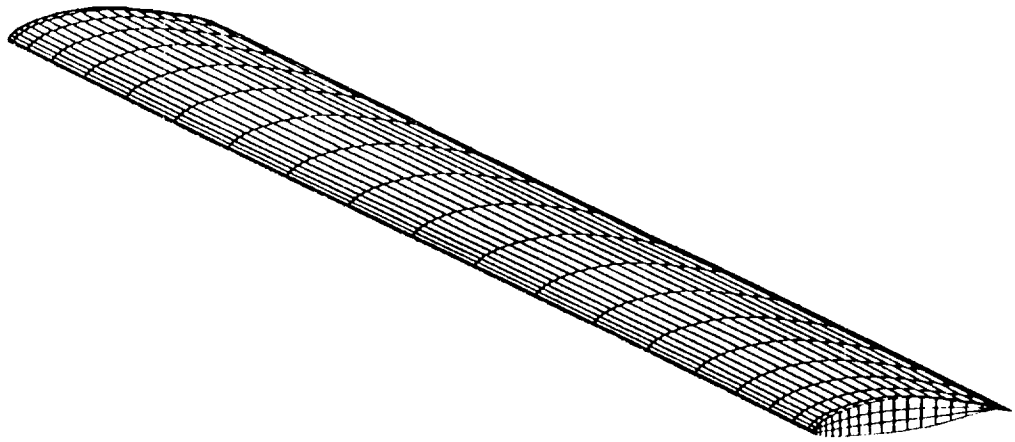

Figure 4.1 Surface Grid Representation of The Generating Wing

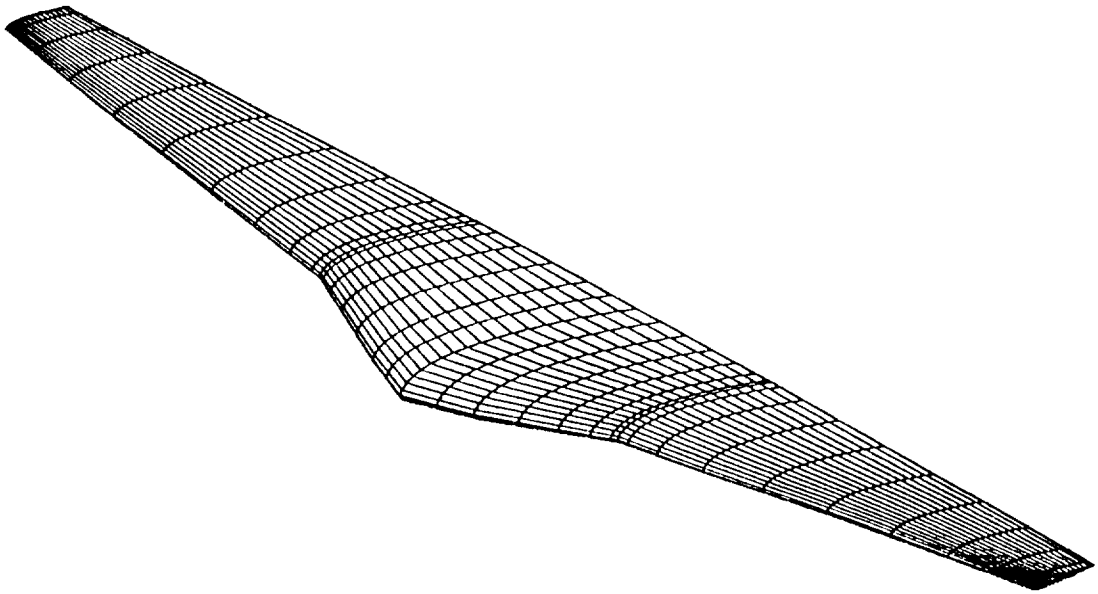

Figure 4.2 Surface Grid Representation of the Following Wing

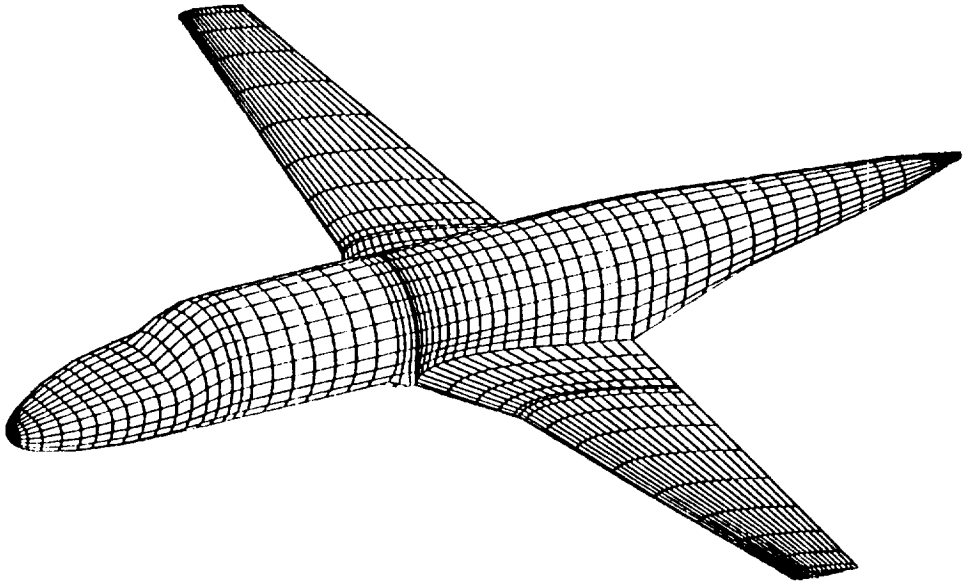

Figure 4.3 Surface Grid Representation of the Following Configuration Without Empennage and High-lift System

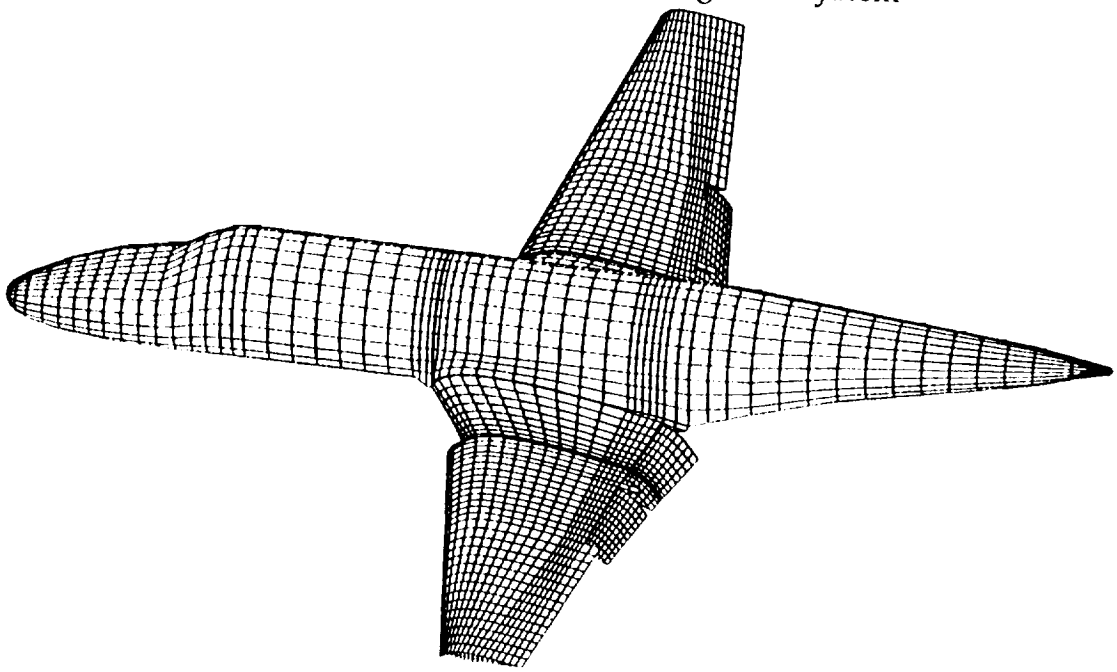

Figure 4.4 Surface Grid Representation of the Following Configuration Without Empennage. Trailing-Edge Flaps Deflected At 35°

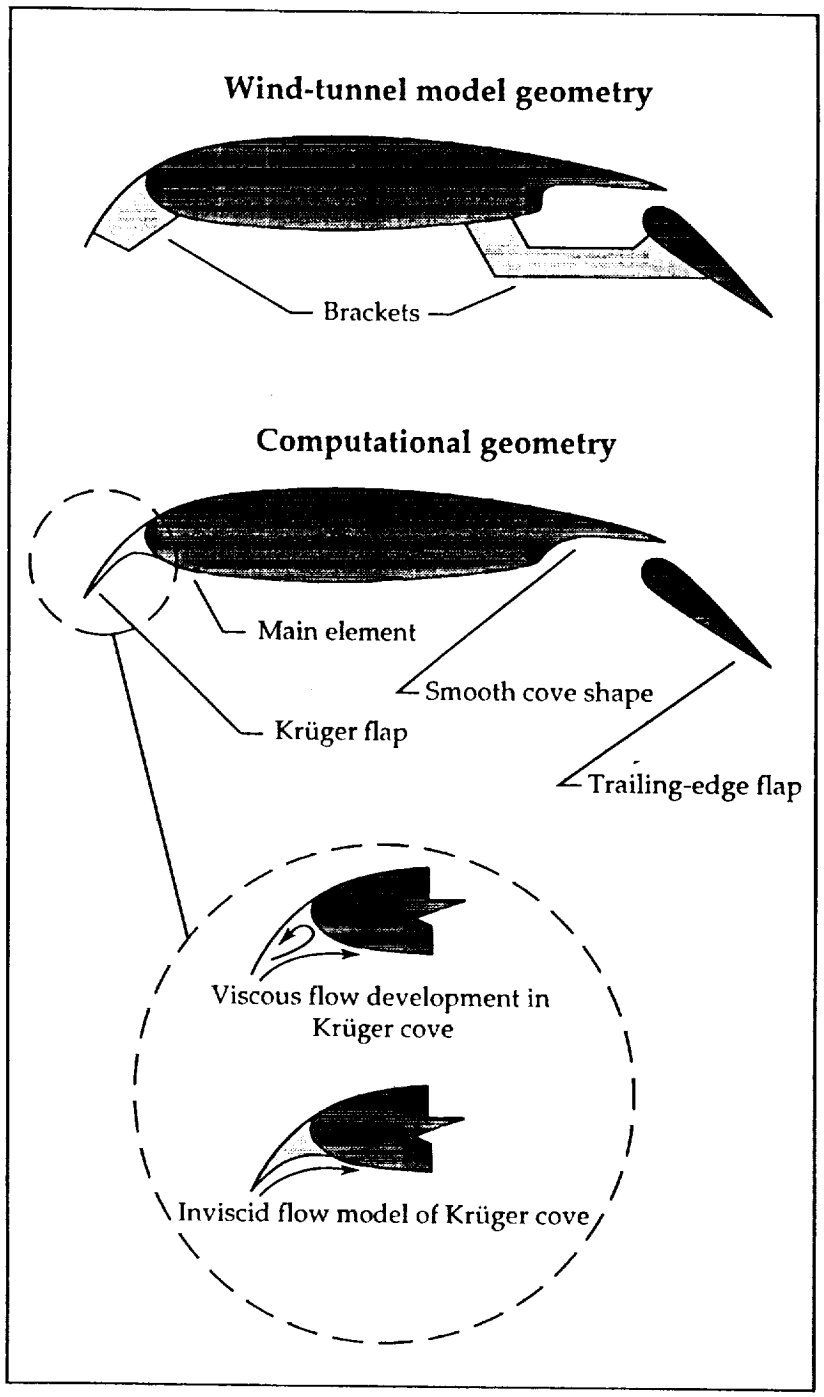

Figure 4.5 Differences Between Computational Geometry and Wind-Tunnel Model Geometry

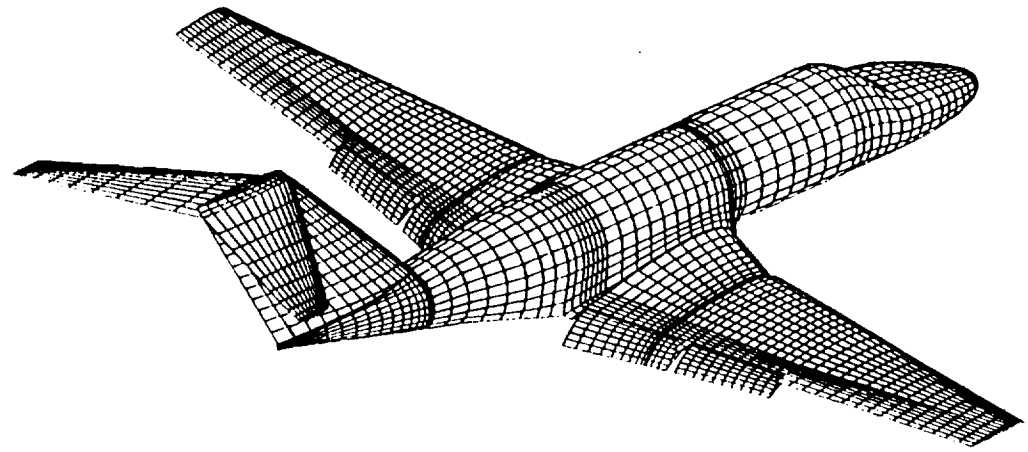

(a)

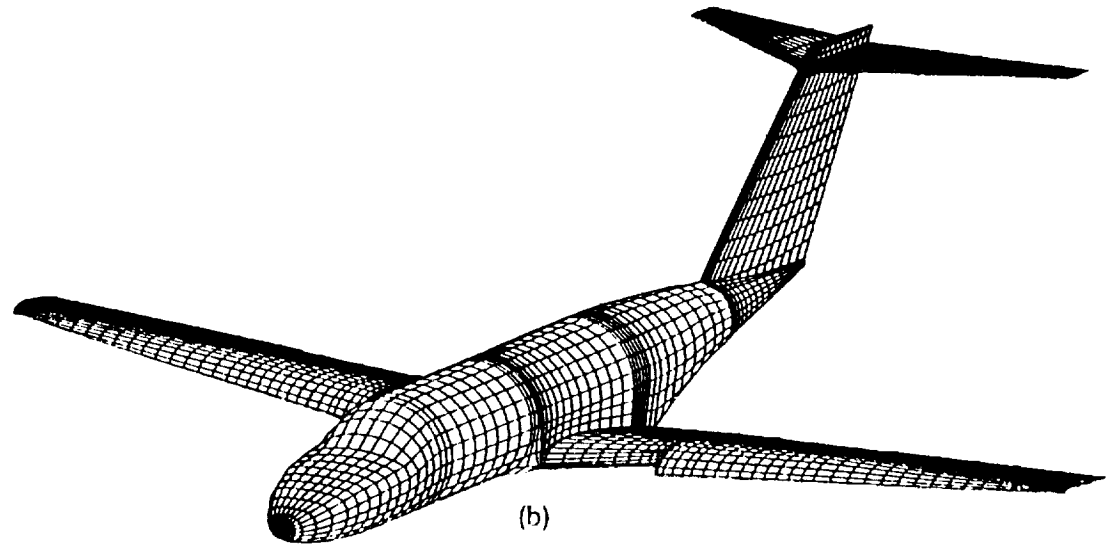

(b)

Figure 4.6 Surface Grid Representation of Complete Following Configuration a) rear view (b) front view

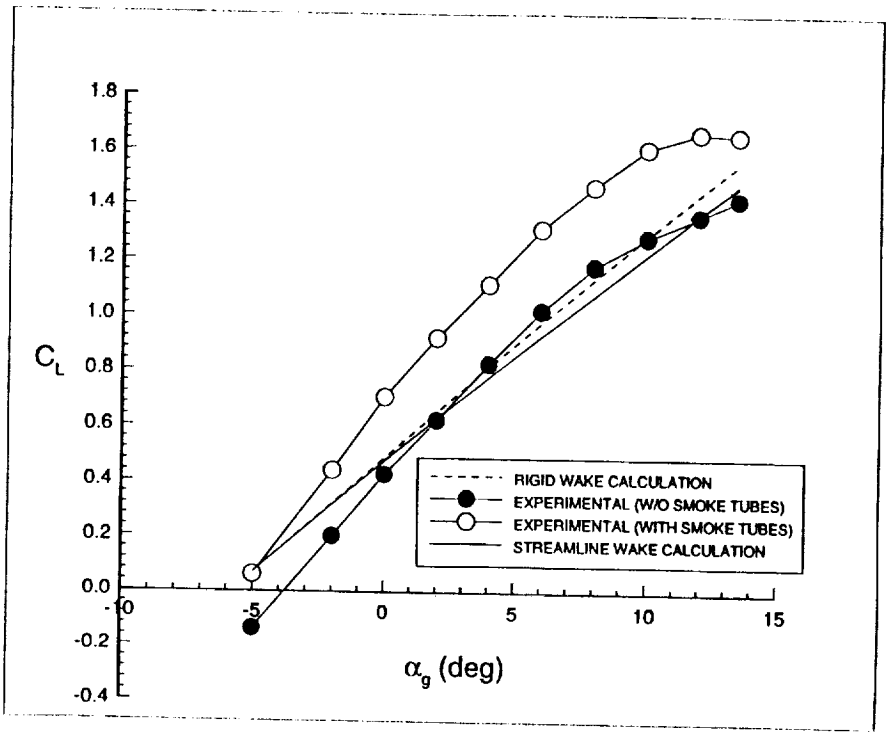

Figure 4.7 Comparison of Measured and Predicted Lift Curves for The Generating Wing

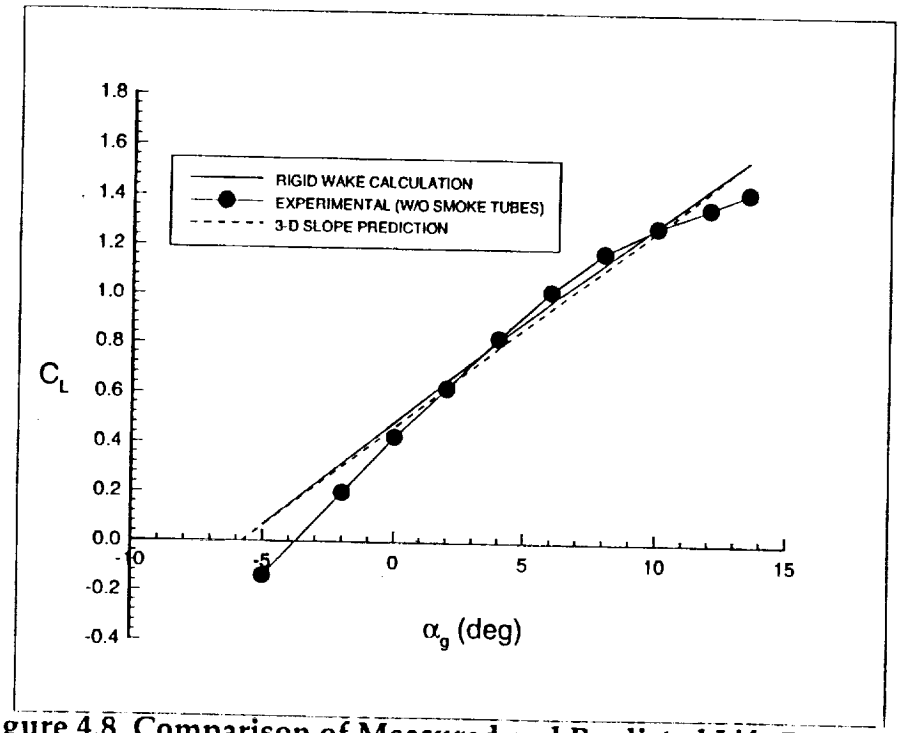

Figure 4.8 Comparison of Measured and Predicted Lift Curves for The Generating Wing with Lifting-Line Theory

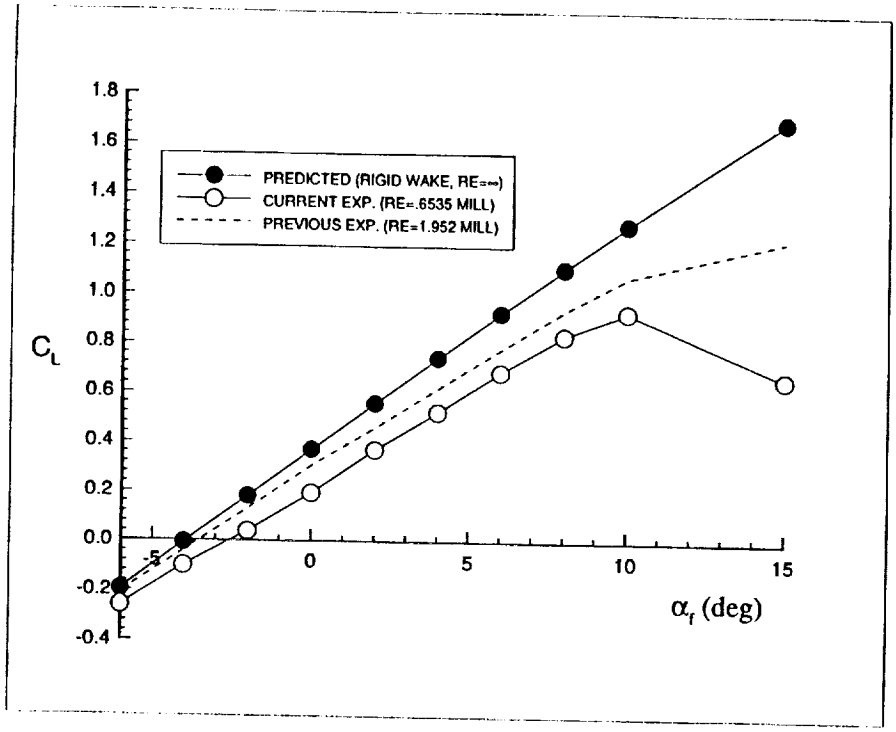

Figure 4.9 Comparison of Measured and Predicted Lift Curves for the Following Wing-Body Configuration at Various Reynolds Numbers

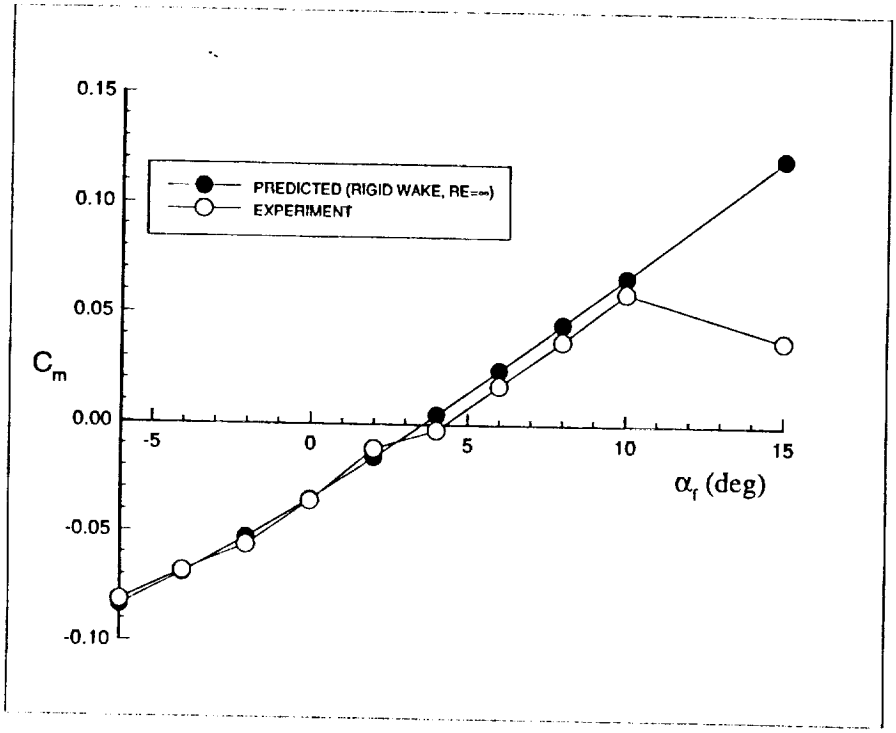

Figure 4.10 Comparison of Measured and Predicted Pitching-Moment Curves for the Following Wing-Body Configuration

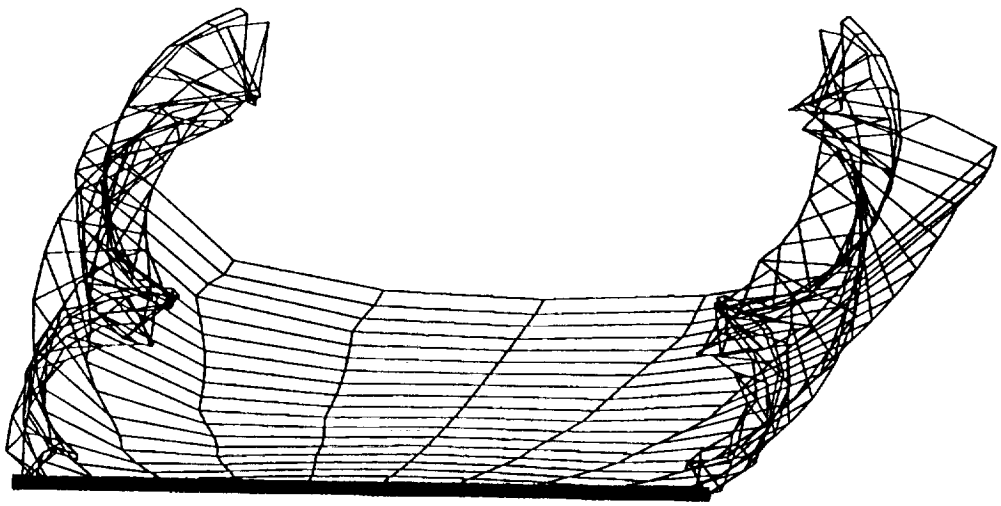

Figure 4.11 Generating Wing with Streamline-Based Wake (C_L=0.94)

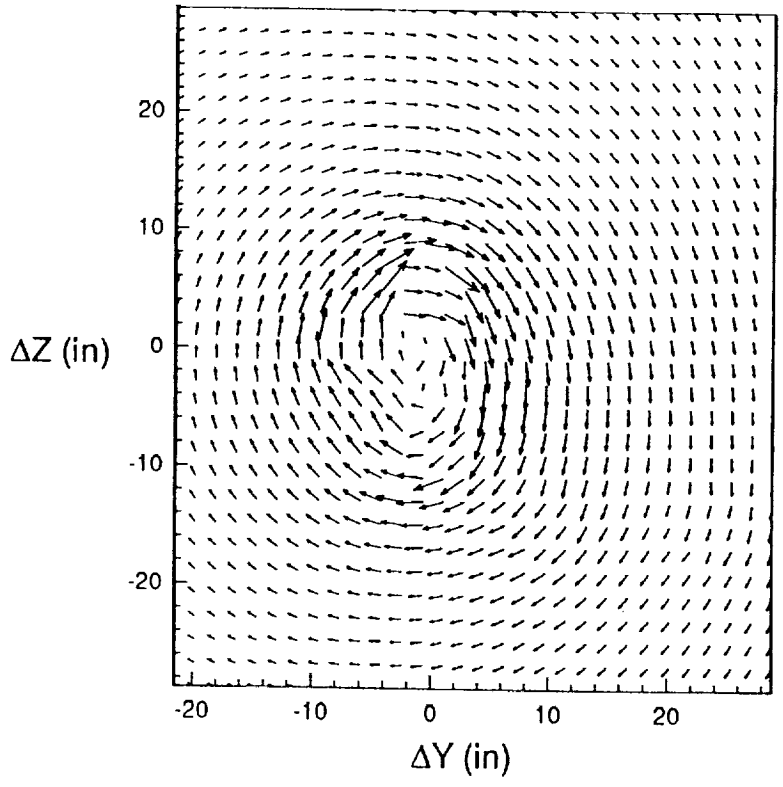

Figure 4.12 Streamline Wake Velocity Vectors (x/b=1.28)

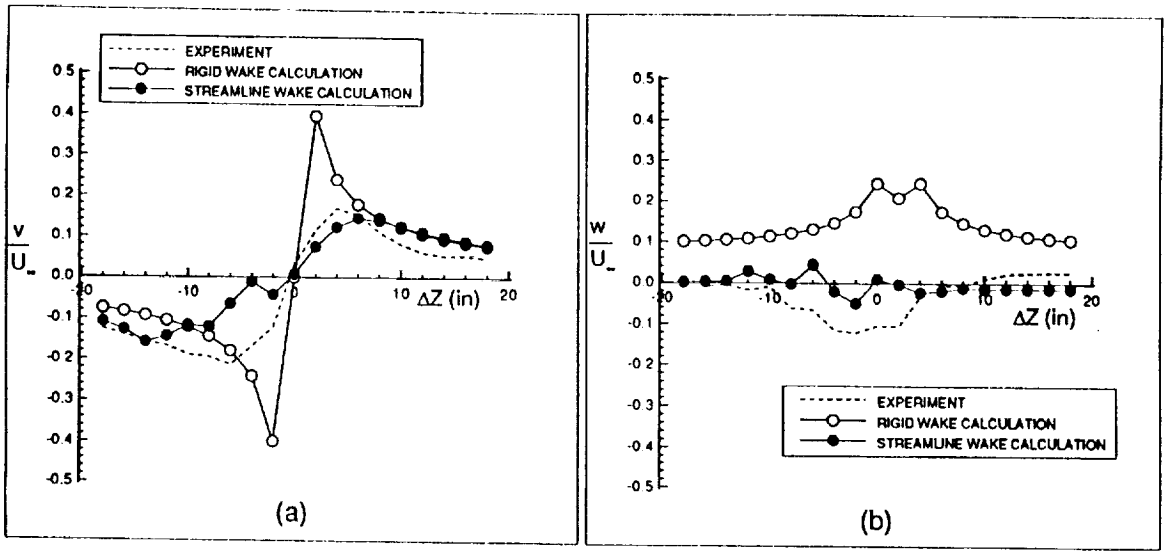

Figure 4.13 Vortex Velocity Comparisons as a Function of ΔZ (ΔY=0)
(a) Sidewash Comparison (b) Upwash/Downwash Comparison

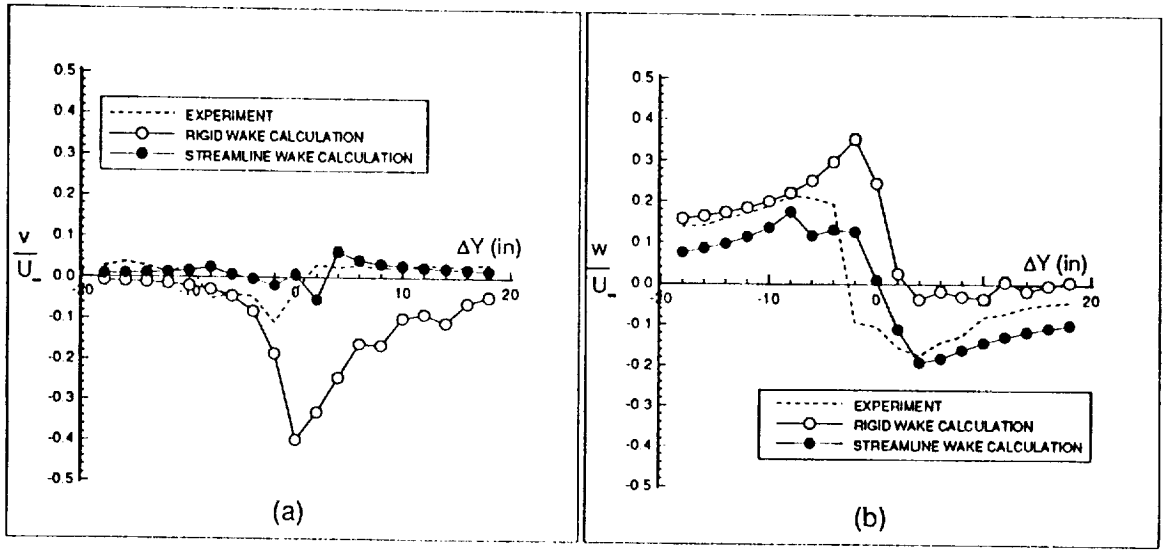

Figure 4.14 Vortex Velocity Comparisons as a Function of ΔY (ΔZ=0)
(a) Sidewash Comparison (b) Upwash/Downwash Comparison

5.0 Vortex-Encounter Comparisons with Experimental Data

Comparisons with experimental data concentrated on only one vortex circulation strength corresponding to a C_L of 0.94 for the generating wing. One lift coefficient comparison was deemed to be sufficient in determining the validity of the code to model the wake-vortex interaction phenomenon. To further simplify the research and reduce the amount of CPU time involved, only zero side-slip angle cases were modeled for the following business-jet model. Moreover, a limitation of the panel method required all interaction comparisons to be conducted at a $\Delta Y = 0.0$ in.. In varying the horizontal distance from the vortex core, ΔY ($\Delta Z = 0.0$ in.), the wake lines of the generating wing would penetrate the surface panels of the following model producing erroneous results. Therefore, the distance between the following model and the vortex core was limited to ΔZ cases only ($\Delta Y = 0.0$) at which the following model was placed either above or below the wake lines. For each ΔZ distance, the α_f of the following model was varied, ranging from -6° to 15°. No more than 1 hour of CPU time for the Cray Y-MP was required to obtain solutions for each computational run of the wake-vortex interaction.

5.1 Lift of the Generating Wing

Although this particular study concentrated on the aerodynamic characteristics of the following model, the C_L of the generating wing was constantly monitored for each computational run. This was accomplished to maintain C_L at its necessary value. The presence of the following model was discovered to have a slight effect on the C_L of the generator. The values for the C_L of the generating wing fluctuated between 0.935 and 0.947. In the wind-tunnel experiment, fluctuations in C_L were also monitored for each run and corrected accordingly by adjusting α_g when necessary. In the

computations, the changes in C_L of the generating wing as a result of varying α_f of the following model were very small. Therefore, the generating wing was kept at a constant α_g in the computations instead of adjusting α_g for a constant C_L at every single run. This, in turn, allowed for a more efficient computation process.

5.2 Aerodynamic Characteristics of the Following Business-Jet Model During Wake-Vortex Encounter

Total force and moment coefficients were calculated for the following business-jet model and compared to experimental results. Comparisons were made at ΔZ values of ± 20, ± 40, +60, and -48.4 inches ($\Delta Z/b = \pm 0.139$, ± 0.278, +0.417, and -0.336) from the vortex core. As mentioned earlier, a positive ΔZ value corresponds to the generating wing being stationed below the following model, and similarly a negative ΔZ value corresponds to the placement of the generator above the following configuration. Experimental data for a ΔZ of -60 inches ($\Delta Z/b = -0.417$) were not obtained due to limitations in the position of the strut mounting system for the generating wing.

In order to accurately correlate the experimental results with the computational solutions, it was ensured that total lift and pitching-moment coefficients were compared at the same axes system. The wind-tunnel experiment employed the wind-tunnel stability axes system to measure the longitudinal force and moment coefficients and the body-axes system to measure the lateral-directional force and moment coefficients. Due to the unique set-up required in modeling the wake-vortex interaction, the computations were limited to the wind-axes system. A detailed description of the transformation of the computed results from the wind-axes system to the body-axes system is presented in Appendix B.

5.2.1 Vortex Interaction with Following Wing Configuration

As previously mentioned, the computational model of the following business-jet was developed in four stages: a wing-only configuration, a wing-body configuration, a wing-body including the high-lift system configuration, and the complete configuration including the empennage. The wake-vortex interaction was modeled for all four stages to obtain a better understanding of the effects of the various aircraft components on this problem. Modeling the following model as a wing-only configuration prior to modeling the entire interaction allowed for an understanding of how to efficiently model the interaction while obtaining the best converged results. The wake-length studies and wing panel density studies discussed earlier, for instance, were performed using the wing-only configuration as the following model. By utilizing the wing-only configuration for the following model, these studies were performed with a minimum amount of paneling and therefore required relatively small amounts of CPU time. The studies performed were consequently more efficient.

The most simple following configuration tested in the wind tunnel to allow for a comparison with the wing-only configuration was that of a wing-body configuration without the high-lift system. Comparison to experimental data was therefore limited to rolling moment since the fuselage was deemed to have a considerable effect on lift, pitching moment, yawing moment and side force as opposed to a slight effect on rolling moment. In an effort to decrease CPU time, computations were performed utilizing the rigid wake on the generating wing for this vortex interaction. Figures 5.1 and 5.2 compare experimental rolling-moment coefficients, C_l, with computed rolling-moment coefficients as a function of α_f for various values of ΔZ. Figure 5.1 displays excellent agreement with experimental data for negative ΔZ

distances. Computed C_l's are shown to exhibit the same trends as the experimental data, such that the rolling moment induced on the following wing is shown to increase as it vertically approaches the vortex core. Moreover, the calculated rolling moment slopes (C_{l_α}'s) are very close to the average rolling moment slopes measured in the wind-tunnel. From Figure 5.1, a relationship between negative vortex distance and C_l can be formed. In particular, Figure 5.1 reveals a decrease in average C_l by 0.01 for every 20 inches ($\Delta Z/b = 0.139$) the following wing moves away from the vortex core.

Figure 5.2a depicts a C_l comparison for positive values of ΔZ. Although the same trends are seen, the computed values for C_l do not show good agreement with experimental data at α_f's greater than -2° for a ΔZ of +40.0 in. and +60.0 in ($\Delta Z/b = 0.278, 0.417$) and at α_f's greater than -4° for a ΔZ of +20.0 in. ($\Delta Z/b = 0.139$). At first glance, Figure 5.2a can be deceiving in that the absolute difference between the calculated values and the experimental values decreases as ΔZ is increased. This appears to suggest that errors decrease as the generating wing moves closer to the ground board. However, taking the percent difference at an α of 8° shows the opposite result -- that the errors increase as the distance to the ground board is decreased. Table 5.1 reveals the increase in C_l error for the following wing, as the generating wing moves closer to the ground board.

ΔZ (in)	%Error
20	33.75
40	51.12
60	56.10

Table 5.1 Relative Error in Prediction of Rolling Moment For the Following Wing Configuration Due to Ground Effect Imposed on the Generating Wing

From Table 5.1, the difference between calculated and experimental results appears to be caused by ground effect affecting the development of the wake of the generating wing. When a lifting surface is close to the ground, the ground will interfere with the development of its trailing vortex system reducing downwash and induced drag, and increasing lift. This ground effect will affect the perturbation velocities produced by the trailing vortex system, thereby affecting the velocity flow field around the following configuration. The influence of ground effect on the structure of vortical wakes has been widely studied.[40,41,42,43] From these investigations, it was discovered that ground effect restricts the vertical development of the wake, hence promoting a spanwise spreading of the wake. The wake interacts viscously with the ground subsequently reducing its strength more rapidly. Hence, wake interaction with the ground reduces the rolling moment induced on a follower aircraft over that induced by the same vortex wake left to decay out of ground effect. According to Smith[44], essentially no ground effect is felt at a height to span ratio, h/b, greater than 1.0. Ground effect becomes significant, however, at a height less than or equal to the semispan of the wing (h/b = 0.5). At a ΔZ of +20 inches ($\Delta Z/b = 0.139$), the generating wing was approximately 6.3 feet from the ground board, and at a ΔZ of +60 inches ($\Delta Z/b = 0.417$), the ground board was only 3.0 feet away. The generating wing has a span of 12 feet, producing an h/b between 0.53 and 0.25 as it traversed downward away from from the vortex core.

In the wind-tunnel experiment, the ground board was located 8 feet below the fixed center of gravity of the following configuration. To account for ground effect, the ground board was numerically modeled at this distance. As expected, this addition yielded better results by shifting the C_l curve downwards. However, computational results still did not accurately portray

the wind-tunnel data as revealed in Figure 5.2b. This discrepancy was probably due to the interaction between the generated vortex wake and the boundary layer formed along the ground board which can not be modeled by the inviscid prediction code. This probablility is further increased once surface roughness effects, high temperatures and wake-vortex descent in the wind-tunnel are taken into account. The set-up in the wind-tunnel with respect to the ground board is depicted in Figure 5.3.

In all, due to the poor correlation between computational and experimental results at distances close to the ground as discussed above, comparisons between computed and experimental results will only be performed for negative ΔZ values. The comparisons in the following sections will hence be based on ΔZ values of -20.0, -40.0 and -48.4 inches ($\Delta Z/b$ = -0.139, -0.278, -0.336) from the vortex core.

5.2.2 Vortex Interaction with Following Wing-Body Configuration

Once the modeling limitations for this wake-vortex interaction problem were established, the fuselage was added to the following model. Computed results were compared to the aerodynamic characteristics of the wing-body configuration obtained in the wind-tunnel. In an effort to decrease CPU time, initial computations were performed utilizing the rigid wake on the generating wing. With the fuselage in place, comparisons were now extended to lift, pitching moment, yawing moment, and side force. A C_L comparison for various negative ΔZ values is shown in Figure 5.4a. Reynolds number sensitivity is again revealed through the difference in C_{L_α} between computational and experimental results. The interaction is seen to shift both the calculated and experimental C_L-curve downwards by a ΔC_L of approximately 0.1. It is readily apparent, however, that the interaction does not significantly affect C_L within the ΔZ range utilized in the experiment

($-0.278 \leq \Delta Z/b \leq 0.336$). Figure 5.4b displays the comparison for pitching-moment coefficient (C_m). As mentioned earlier, the moment center was shifted 0.72 in. aft for the wing-body configuration to obtain improved results for C_m. The calculated pitch-curve slope, C_{m_α}, is seen to closely match the experimental C_{m_α} up to an α_f of 8°. Like the C_L comparison, varying the distances from the vortex core did not have a significant effect on C_m within the ΔZ range utilized in the experiment ($-0.278 \leq \Delta Z/b \leq 0.336$).

Rolling moment and yawing moment comparisons are presented in Figures 5.4c and 5.4d. The most common parameter used in defining wake-vortex hazard is the rolling-moment coefficient. Computed C_l curves exhibited the same trends as previously revealed in the interaction with the wing-only configuration. The only difference was the increase in calculated C_l due to the addition of the fuselage. This increase was small in that the C_l curve shifted upward by about 3.7%. Like the C_m and C_l comparisons, computed yawing-moment coefficient (C_n) comparisons show good agreement with experimental results up to an α_f of 8°-10° at which flow-separation effects become significant. Figure 5.4d shows an increase in the slope of the yawing-moment coefficient with α_f as the distance to the vortex core is reduced. An increase in slope indicates a larger yawing-moment magnitude imposed on the following configuration. From the computational results, it was found that at low α_f's, the majority of the total yawing moment was acquired from the pressure gradients on the forebody as pictured in Figure 5.5. Here, pressure contours are depicted for the following wing-body forebody at a ΔZ of -20.0 in. ($\Delta Z/b = -0.139$) for various α_f's. Larger suction pressures are seen on the left forebody than on the right forebody due to the predominantly negative sidewash velocities located below the vortex. The resulting pressure gradient on the forebody indicates a negative yawing moment. The suction

pressures are seen to decrease with increasing α_f. As α_f is increased, pressure gradients on the mid fuselage, near the fuselage-wing juncture, also increase as seen in Figure 5.6. At higher α_f's, these pressure gradients become a larger factor in defining the yawing moment than the forebody pressure gradients. Therefore, as α_f is increased, the total yawing moment magnitude increases with a positive increment.

Finally, Figure 5.7 shows the comparison for the side-force coefficient, C_Y. Unlike the previous moment comparisons, computational results did not immediately correspond to wind-tunnel results for the C_Y comparison. In particular, calculated magnitudes for C_Y were as small as 1/3 of experimental values. In addition, calculated C_Y-α_f slopes were negative as opposed to the positive slopes obtained in the wind tunnel. The wind-tunnel experiment, however, is shown to have some model asymmetries and/or flow angularities associated with it as indicated in the experimental case without the vortex being impinged on the following model (Figure 5.7a). For this experimental "no vortex" case, a significant C_Y discrepancy of -0.01 is shown at an α_f of -6°. This discrepancy decreases as α_f is increased. These ΔC_Y biases were subtracted from every experimental ΔZ case with the assumption that these asymmetric biases were consistent for every run. The comparison utilizing the corrected C_Y values are shown in Figure 5.7b. Experimental slopes exhibit good correlation with calculated slopes. In particular, C_Y values for the ΔZ cases of -40.0 in. and -48.4 in. ($\Delta Z/b$ = -0.278, -0.336) show very good agreement. Poor agreement for the ΔZ case of -20.0 in. ($\Delta Z/b$ = -0.139), however, indicates either unmodeled phenomena in the experimental data or an inaccurate calculation of sidewash velocities at distances close to the vortex core.

In order to investigate the accuracy of the sidewash velocity calculations based on the rigid wake technique, a second set of calculations were performed

using the streamline-based wake technique on the generating wing. As depicted earlier in Figure 4.13a, sidewash velocities created by the rigid wake at -18.0 in. ($\Delta Z/b$ = -0.125) from the vortex core were approximately 30% less than the velocities produced by the streamline-based wake. Upwash velocities were also overpredicted by the rigid wake method as seen in Figure 4.13b. These discrepancies, however, did not affect all of the aerodynamic characteristics. In utilizing the streamline-based wake method, significant variations from the rigid wake method were only exhibited in rolling moment and side force as shown in Figure 5.8. Unlike the rigid wake, the streamline-based wake has the ability to capture wake descent. Because of this capability, the -20.0 in. ΔZ case ($\Delta Z/b$ = -0.139) was unable to be modeled. At this distance, the wake lines penetrated the fuselage panels producing erroneous results. Therefore, calculations were performed for the smallest feasible distance of -30.0 inches ($\Delta Z/b$ = -0.208) in order to verify the ability of the streamline-based wake method to produce a more accurate velocity field than the rigid wake method at small distances from the vortex core. C_l curves for a ΔZ of -30.0 , -40.0 and -48.4 in. ($\Delta Z/b$ = -0.208, -0.278, -0.336) are displayed in Figure 5.8a for both the rigid wake and streamline-based wake techniques. All curves based on the streamline-based wake technique exhibit a consistent yet insignificant C_l increase of approximately 0.001 over the rigid wake technique. Unlike C_l, C_Y is seen to be very dependent on distance and wake technique. As expected, C_Y values remained unaffected by the two different wake techniques at the larger ΔZ distances of -40.0 and -48.4 in. ($\Delta Z/b$ = -0.278, -0.336). However, at a ΔZ of -30.0 in. ($\Delta Z/b$ = -0.208) the discrepancy in the sidewash and upwash velocities between the two techniques is clearly visible as indicated in Figure 5.8b. Unfortunately, experimental results were not obtained at this distance to allow for a comparison. A picture of the

wake-vortex interaction utilizing the streamline-based wake for the generating wing is illustrated in Figure 5.9 for a ΔZ of -48.4 in. ($\Delta Z/b$= -0.336).

5.2.3 Vortex Interaction with Following Wing-Body Configuration with High-Lift System

Although results for the interaction between the generating wing and the following wing-body configuration are well predicted, a comparison with the high-lift system attached to the following configuration is necessary to model the take-off and landing configurations associated with this complex problem. The effect of the high-lift system on experimental and calculated C_L and C_m values is shown in Figure 5.10. As expected, the addition of the high-lift system increases C_{Lmax} and produces a more negative α_o without significantly changing the lift-curve slope, C_{L_α}. However, the shift in the lift curve, ΔC_L, is overpredicted by the inviscid method with a ΔC_L of approximately 0.80 as opposed to an average ΔC_L of 0.50 for the experimental results. According to Lan and Roskam[45], at full-scale Reynolds numbers, a flap deflection (δ_f) of up to 15° can be incurred on most commonly used wing sections before flow separation occurs on the surface. The current δ_f setting of 35° in conjunction with the low-Reynolds number conditions in the wind-tunnel experiment probably cause significant flow separation. This flow separation could be a large contributing factor to the discrepancies between experimental and calculated lift values.

The effect of the addition of the high-lift system on C_m is shown in Figure 5.10b. Here, C_m values are shown with and without the 0.72 in. moment center correction. For the wing-body configuration, a slight shift in the moment center had a significant effect on the pitching moment since the aerodynamic center was adjacent to the moment center. Adjustment of the moment center resulted in improved values for C_m for this particular

configuration. As expected, the increase in camber due to the addition of the high-lift system produced a negative increment for both the experimental and calculated C_{m_o}. The experimental C_{m_o} is seen to be greater than the calculated value. The shift in C_{m_α} between experimental and calculated results signifies a shift in the aerodynamic center of the configuration. The aerodynamic center of the wing-body configuration was calculated to be 1.36 in. forward of the aerodynamic center calculated for the experimental model. The value for this aerodynamic center shift was the same for the results utilizing both the shifted and unshifted moment centers. This aerodynamic center shift can account for most of the differences between the experimental and computational results. The calculated results are shown to be more unstable than the experimental results due to the increase in negative static margin resulting from the aerodynamic center shift. This shift in the aerodynamic center is most likely due to the differences between the computational high-lift geometry and the actual high-lift geometry as previously pictured in Figure 4.5. Flow separation effects, mentioned earlier, could also result in the differences seen here between the experimental and computational results.

As previously established, the use of the rigid wake produced similar results as the streamline-based wake at ΔZ distances of -40.0 in. and -48.4 in. ($\Delta Z/b$ = -0.278, -0.336). These similar results produced by the rigid wake technique coupled with the inability of the streamline-based wake to obtain a comparison at a ΔZ of -20.0 in. ($\Delta Z/b$ = -0.139) due to panel penetration were the basis for the decision to utilize the rigid wake technique for the following comparisons. These comparisons are presented in Figures 5.11 and 5.13. The discrepancies mentioned earlier between experimental and calculated C_L and C_m values are evident in Figures 5.11a and 5.11b. Once again, a loss in lift coefficient of approximately 0.1 for both the computed and experimental

results is observed due to the wake-vortex interaction. Since improved values for C_m were obtained when the moment center was shifted aft for this particular configuration, the 0.72 in. correction was maintained for the interaction between the vortex and this particular configuration without the empennage. As in the previous interaction between the generating wing and the following wing-body configuration, the values for C_L and C_m are not significantly affected within the ΔZ range utilized in the experiment.

Despite the differences in C_L and C_m predictions between experimental and computational results, good comparisons are exhibited for C_l and C_n up to an α_f of 10° as shown in Figures 5.11c and 5.11d. The effect of the high-lift system is more apparent in the rolling-moment comparison as revealed in the almost inverse parabolic shape of the C_l experimental curve as opposed to the calculated linear shape of the C_l curve. Nonetheless, the magnitude of the rolling-moment coefficient is predicted fairly well at ΔZ distances of -40.0 in. and -48.4 in. ($\Delta Z/b$ = -0.278, -0.336). Experimental results show significantly larger non-linearities at the ΔZ distance of -20.0 in. ($\Delta Z/b$ = 0.139) which the present inviscid code can not model. Unlike C_l, values for C_n are well predicted for all three ΔZ distances as indicated in Figure 5.11d. Once again, a positive increase in the yawing moment with α_f is seen for the same reasons previously specified. However, unlike the previous vortex interaction with the wing-body configuration, values for the total yawing moment are not negative at small α_f's. This is because the addition of the high-lift system produces pressure gradients on the mid fuselage which dominate the negative yawing moments produced on the forebody. This is revealed in Figure 5.12 in which pressure contours for the wing-body are compared with and without the high-lift system at an α_f of 0° and a ΔZ = -20.0 in. ($\Delta Z/b$ = -0.139). The larger asymmetrical pressure distributions on the mid fuselage produced by the

addition of the high-lift system cause a positive total yawing moment at low α_f's which increase with increasing α_f.

Reliable C_Y comparisons were limited to the -40.0 in. and -48.4 in. ΔZ case ($\Delta Z/b$ = -0.278, -0.336) due to the inability of the rigid wake to accurately predict wake velocities at a ΔZ of -20.0 in. ($\Delta Z/b$ =-0.139) as evidenced by Figures 4.13b and 5.5b. Once again model asymmetries and flow angularities contributed to the discrepancies in the experimental C_Y values as shown in Figure 5.13a. Therefore, biases were once more removed from these values as displayed in Figure 5.13b. Although trends were similar, the experimental magnitude of C_Y was almost twice that of the computed C_Y at each α_f.

5.2.4 Vortex Interaction with Following Full-Computational Configuration

Finally, computations were performed for the complete following configuration and were compared with wind-tunnel results. These comparisons are presented in Figures 5.14a through 5.14f. The addition of the empennage limited comparisons to ΔZ distances of -40.0 in. and -48.4 in. ($\Delta Z/b$ = -0.278, -0.336). At a ΔZ of -20.0 in. ($\Delta Z/b$ = -0.139), the wake lines of the generating wing penetrated the empennage panels producing erroneous results. A C_L comparison is shown in Figure 5.14a. The high-lift effect on C_L, seen in the previous interaction, is carried over to this particular comparison. In general, the tail does not produce a significant effect on C_L or C_{L_α}. The effect of the tail on C_m, however, is significant as shown in Figure 5.14b. As expected, stability is attained through the addition of the tail as seen from the negative C_{m_α} slope. Calculated C_m values closely match experimental values up to an α_f of 10°. It was not necessary to shift the moment center to obtain a good comparison for C_m. The addition of the empennage resulted in a farther aft aerodynamic center and therefore a larger static margin. Therefore, a slight shift in the moment center had little affect. From the comparisons for C_l, C_n,

and C_Y depicted in Figures 5.14c through 5.14f, it is evident that the computations do not predict the small but distinct non-linear effects produced by the addition of the empennage. These non-linearities are more prevalent in this particular vortex-interaction case as opposed to the previous case without the empennage. A potential contributor to these discrepancies is the differences between the experimental and calculated wake development of the following configuration. Differences in wake development between the experimental model (which has a viscous wake) and the computational model (which employs a rigid inviscid wake) produce differences between experimental and computational velocity flow fields around the tail. Utilizing a streamline-based wake on the following configuration will likely correct for this and should be addressed for further study. Another potential error could be due to a difference between the experimental and computational tail geometry. In all, although all the wake effects can not be modeled, the magnitudes and trends as a function of ΔZ are well predicted.

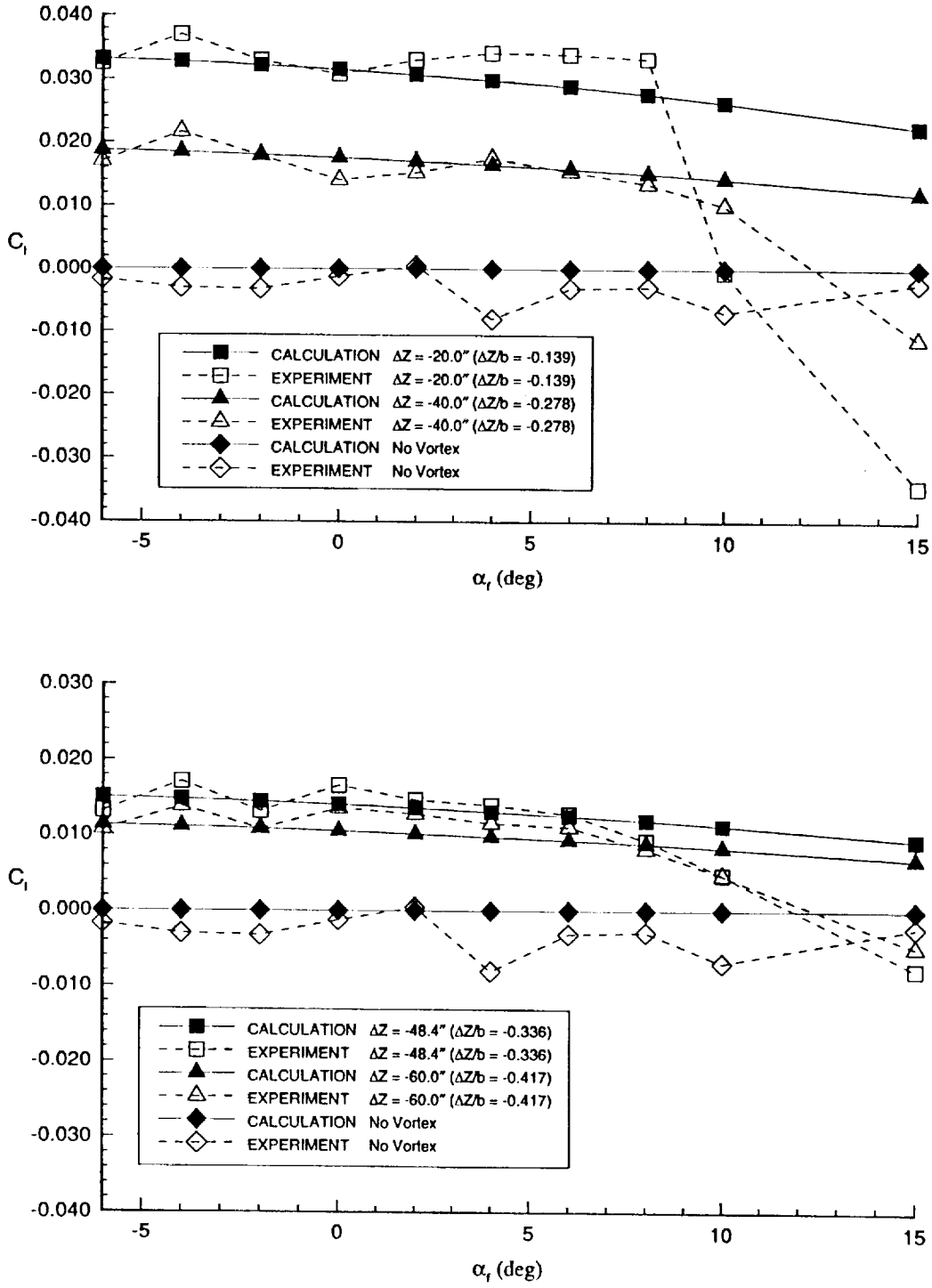

Figure 5.1 Rolling Moment Comparison for Different Negative ΔZ Distances

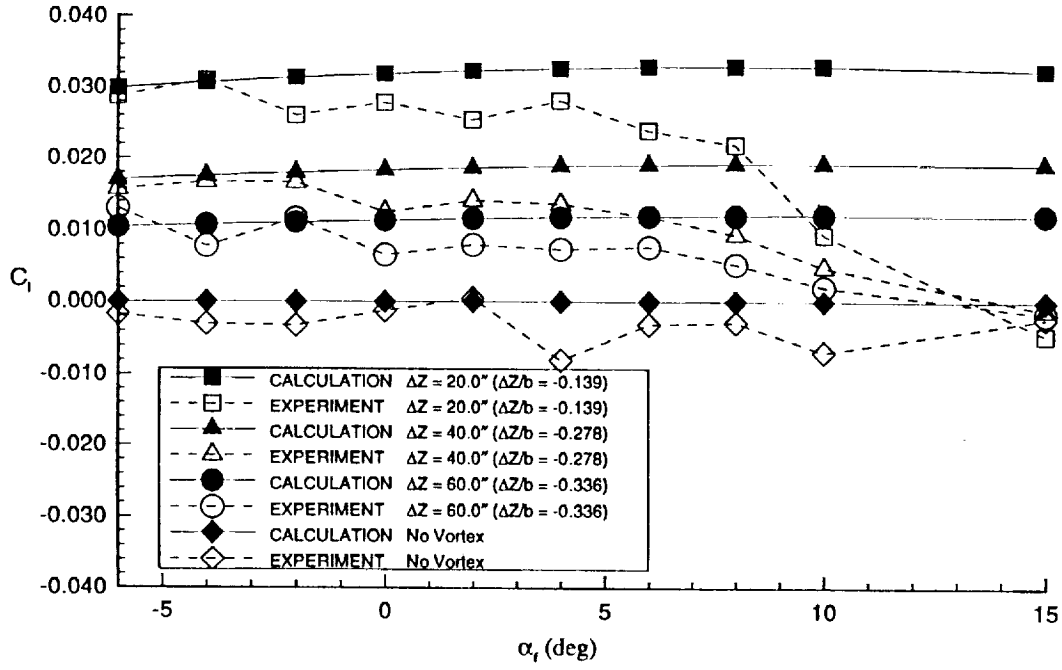

(a)

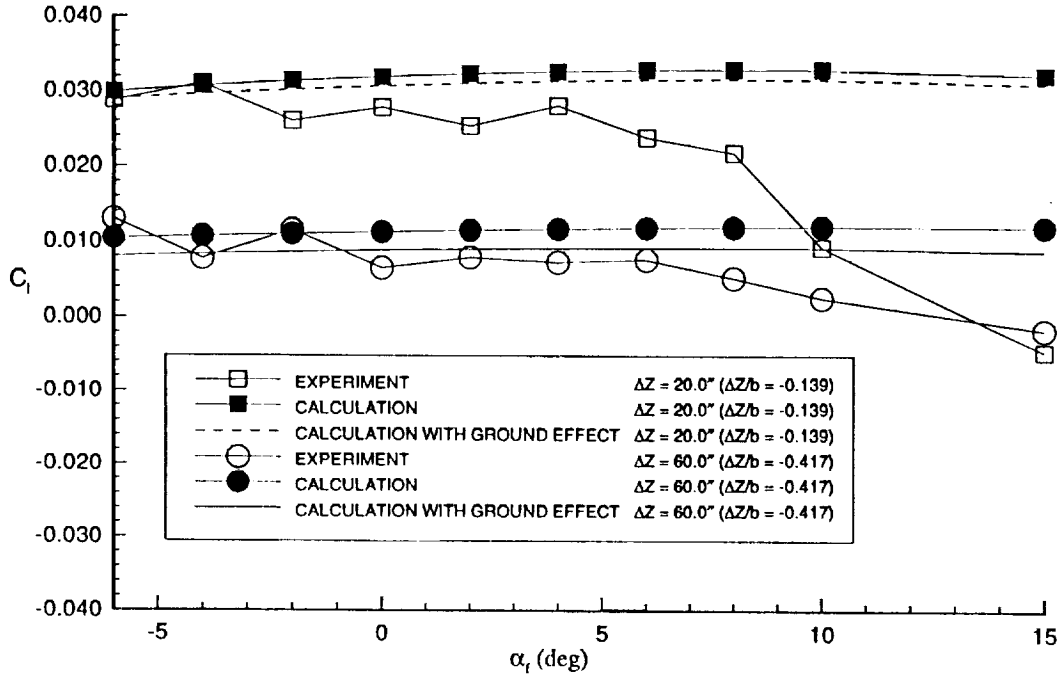

(b)

Figure 5.2 Rolling Moment Comparison for Different Positive ΔZ Distances (a) Computed Results (b) Computed Results with Modeled Ground

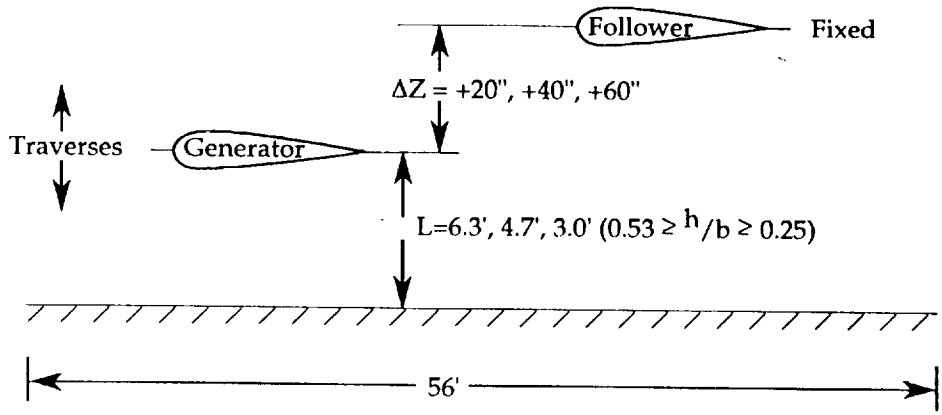

Figure 5.3 Experimental Set-up with Respect to the Ground Board

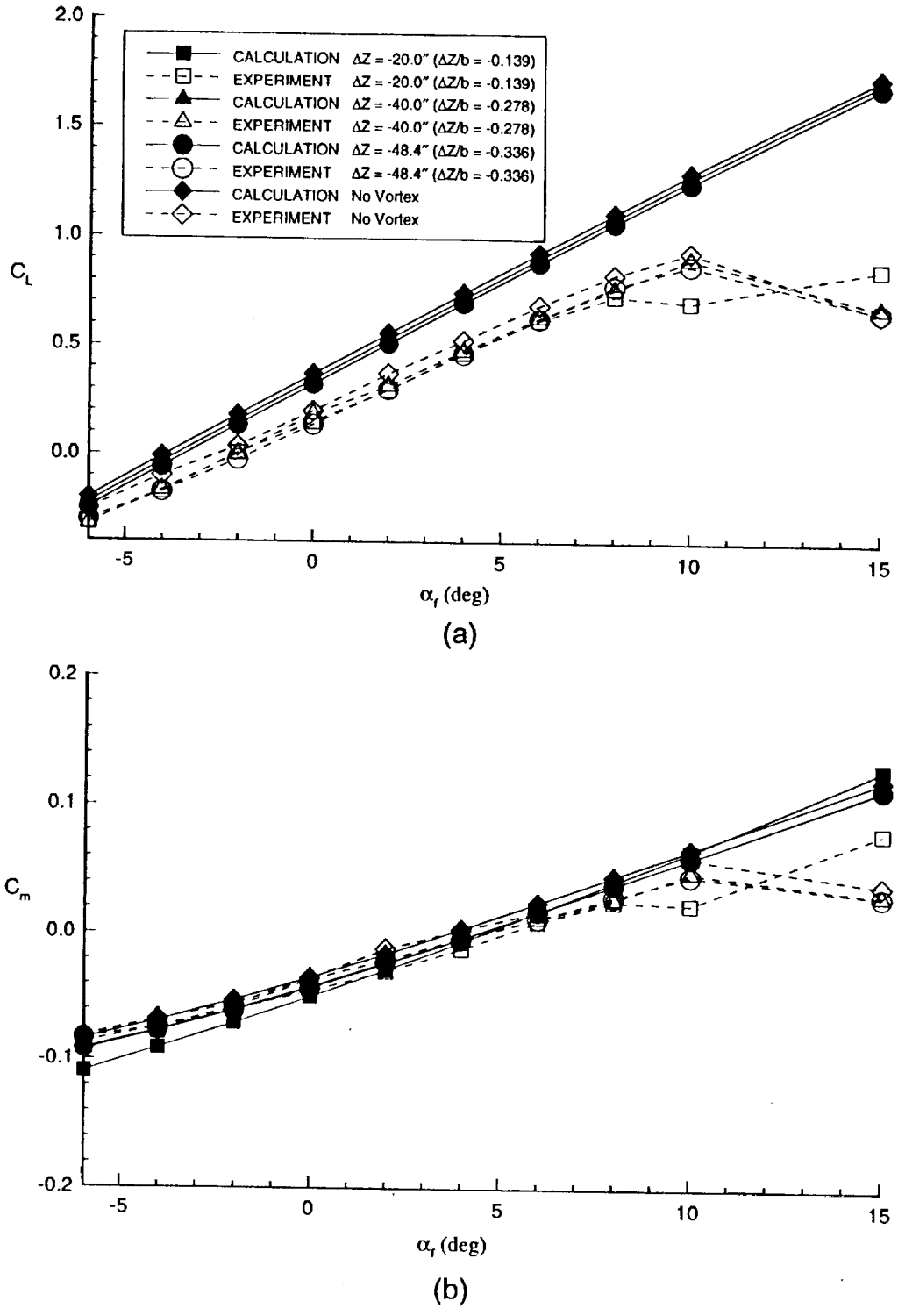

Figure 5.4 Comparison of Aerodynamic Characteristics for the Following Wing-Body Configuration (a) C_L Comparison (b) C_m Comparison

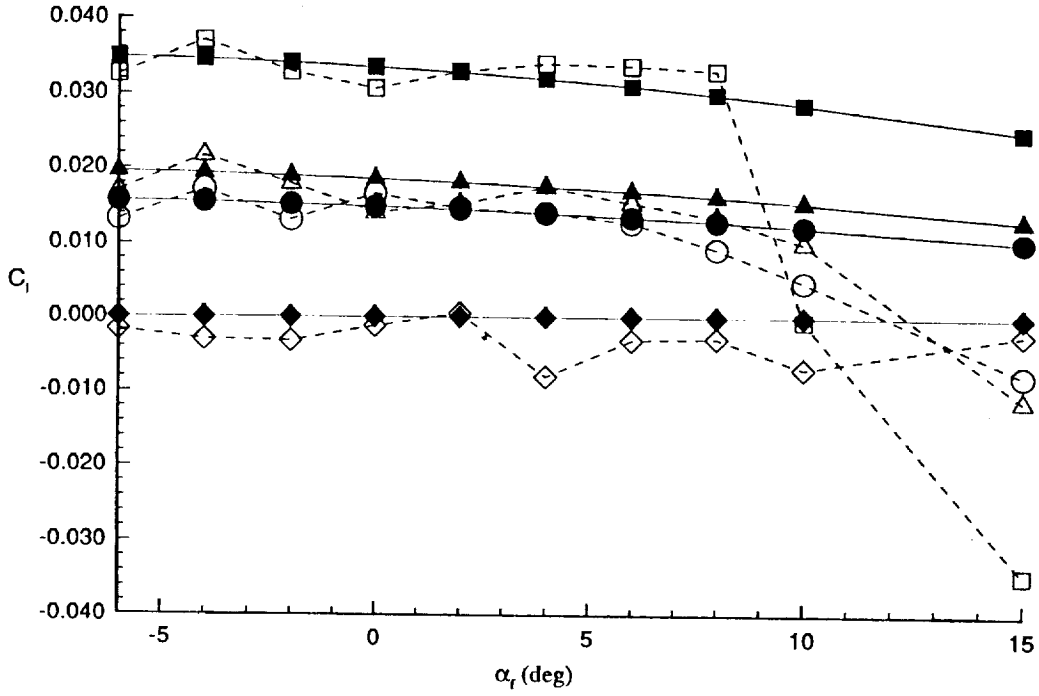

(c)

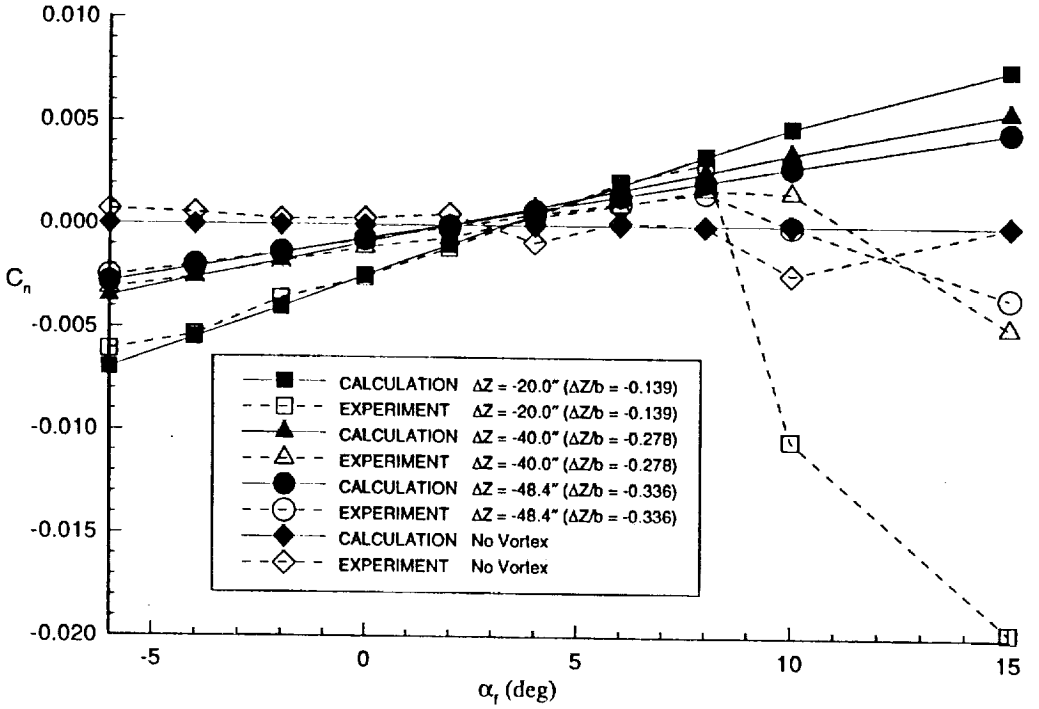

(d)

Figure 5.4 Comparison of Aerodynamic Characteristics for the Following Wing-Body Configuration (c) C_l Comparison (d) C_n Comparison

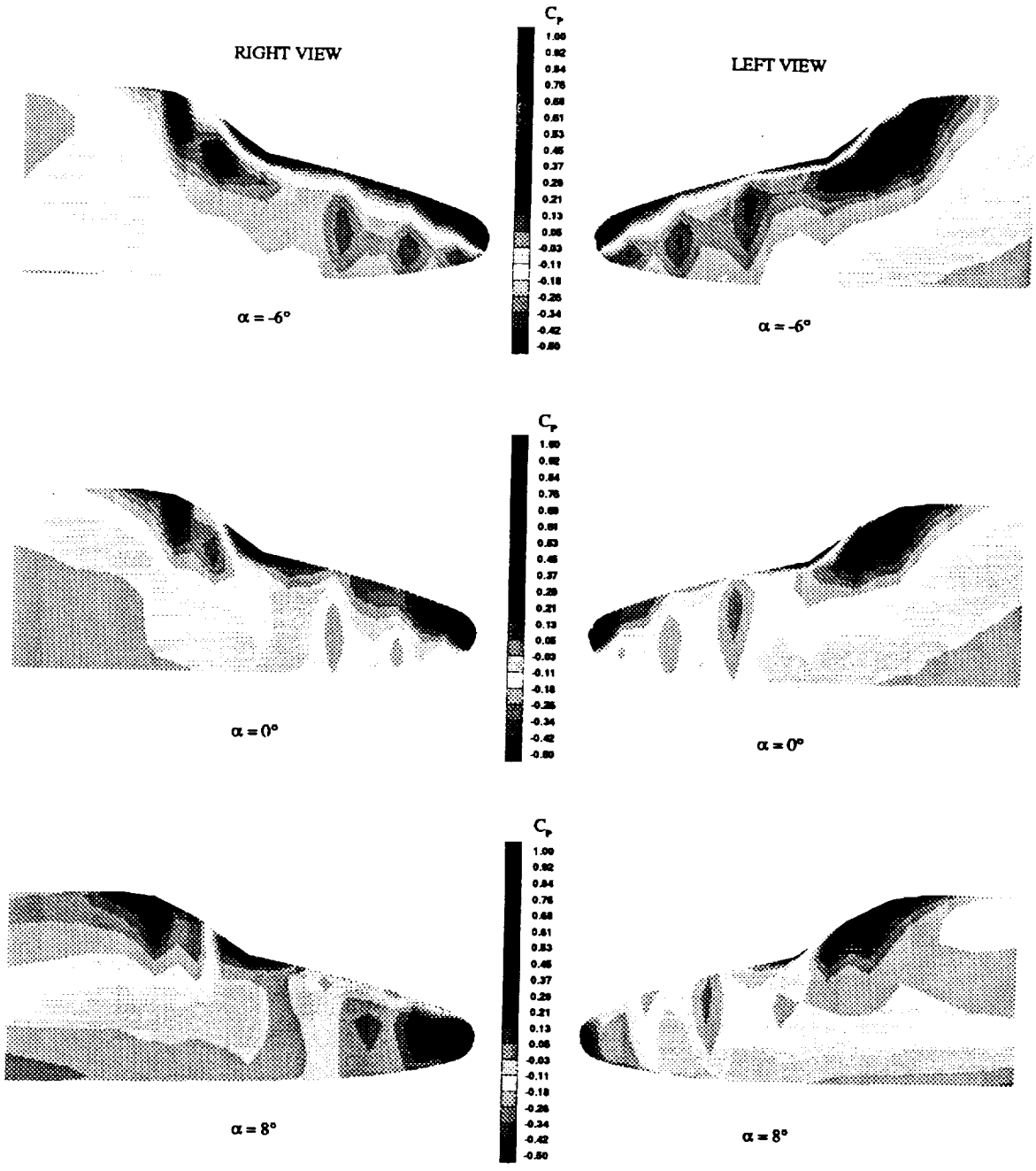

Figure 5.5 Forebody Pressure Contours for the Wing-Body Configuration at Various α_f's (ΔZ = -20.0 in., $\Delta Z/b$ = -0.139)

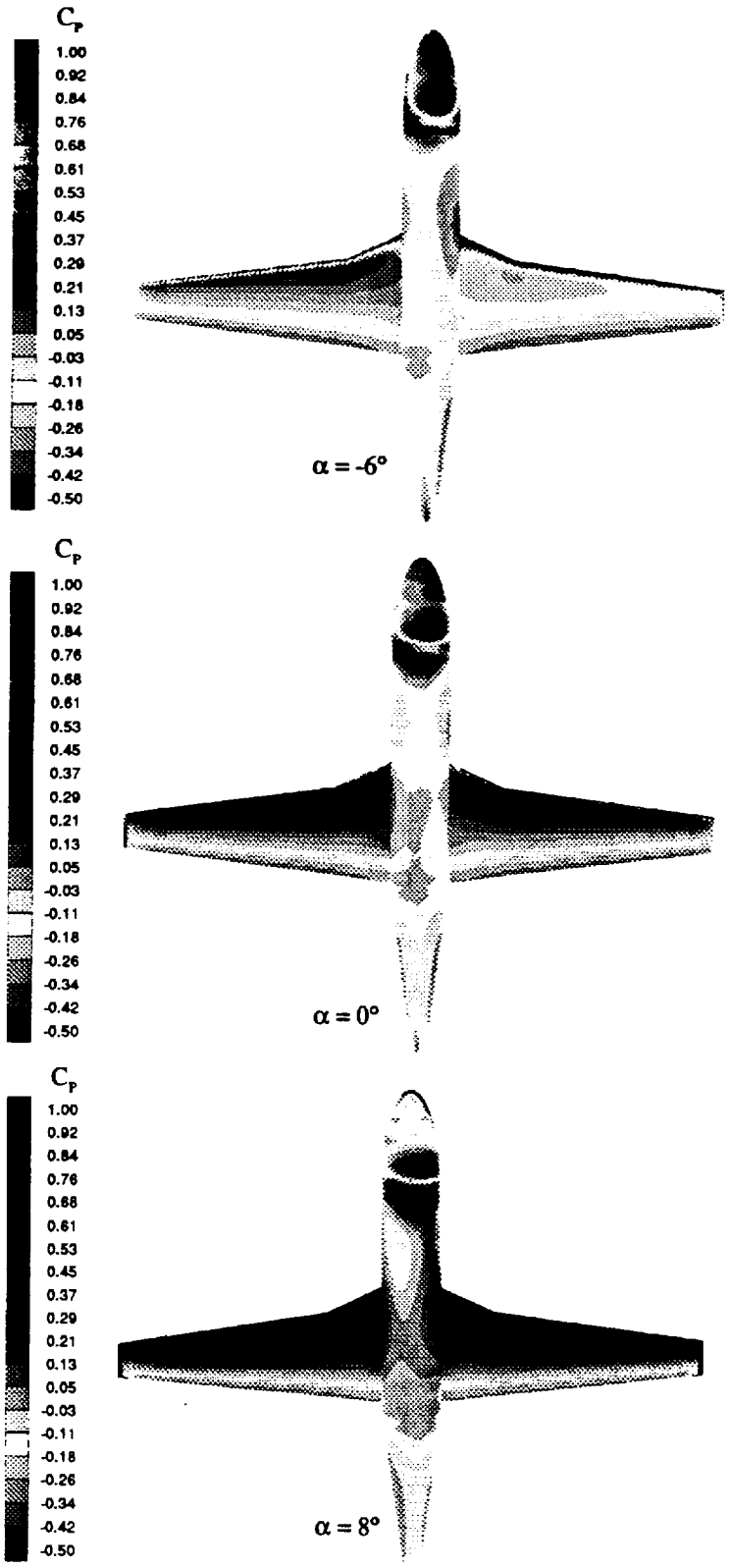

Figure 5.6 Pressure Contours for the Wing-Body Configuration
(ΔZ = -20.0 in., $\Delta Z/b$ = -0.139, top view)

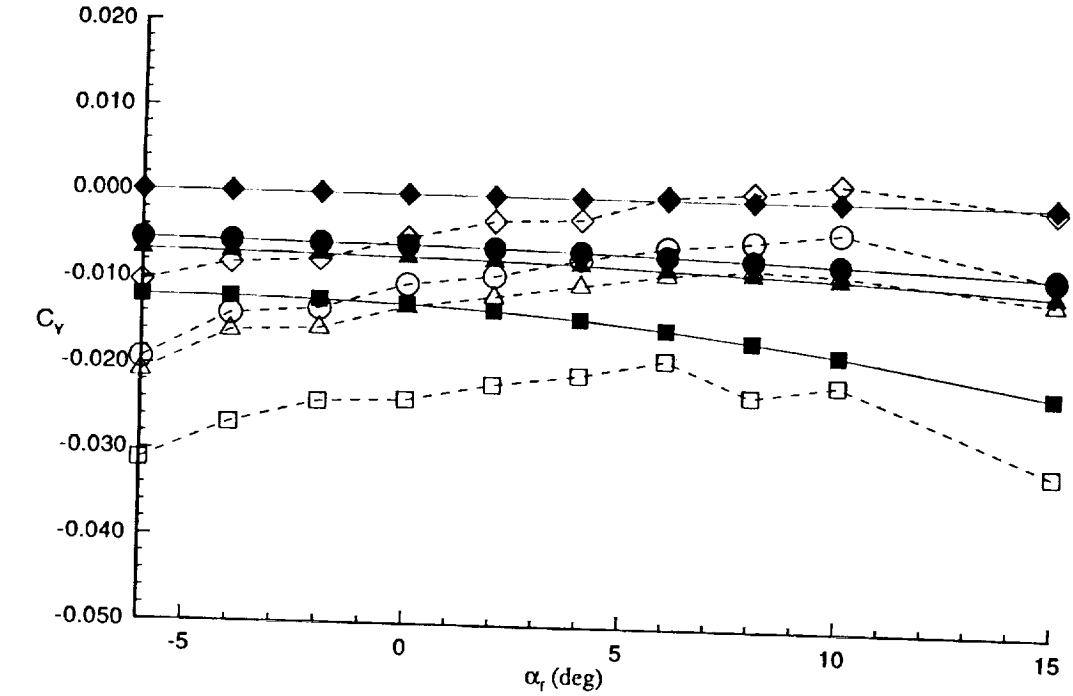

(a)

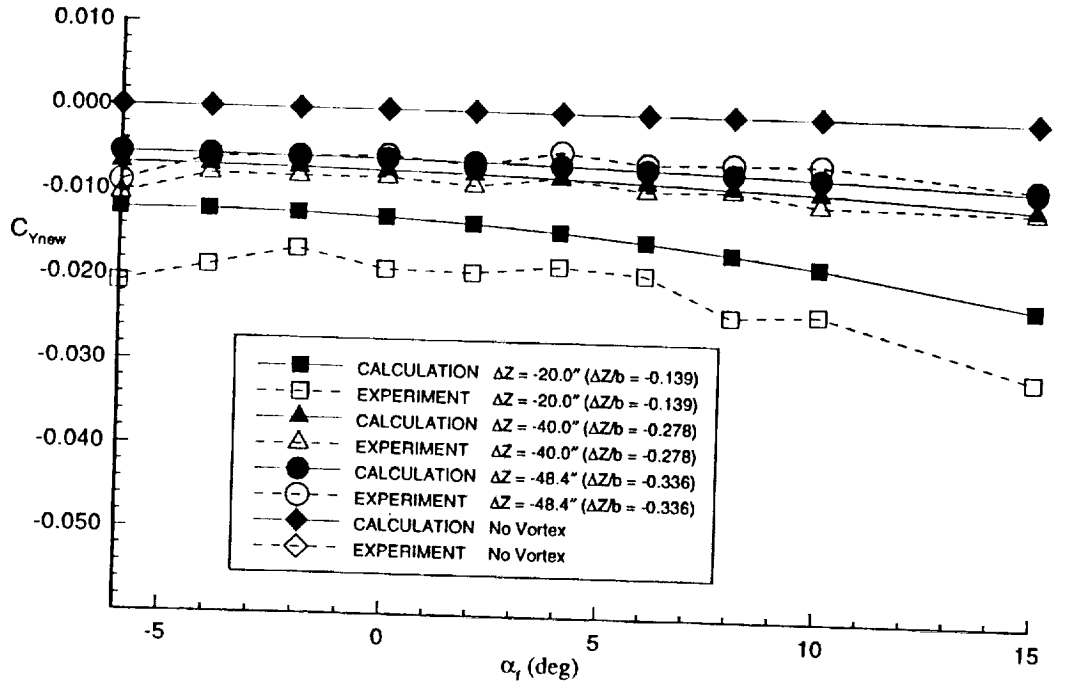

(b)

Figure 5.7 Side Force Comparison for the Following Wing-Body Configuration (a) C_Y Comparison (b) New Unbiased C_Y

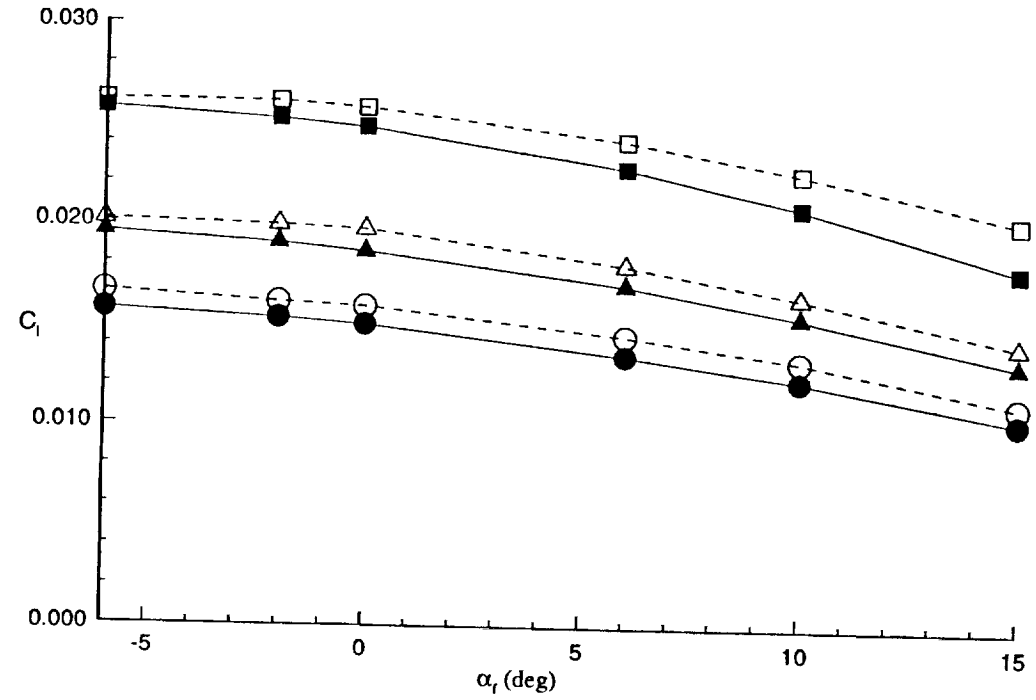

(a)

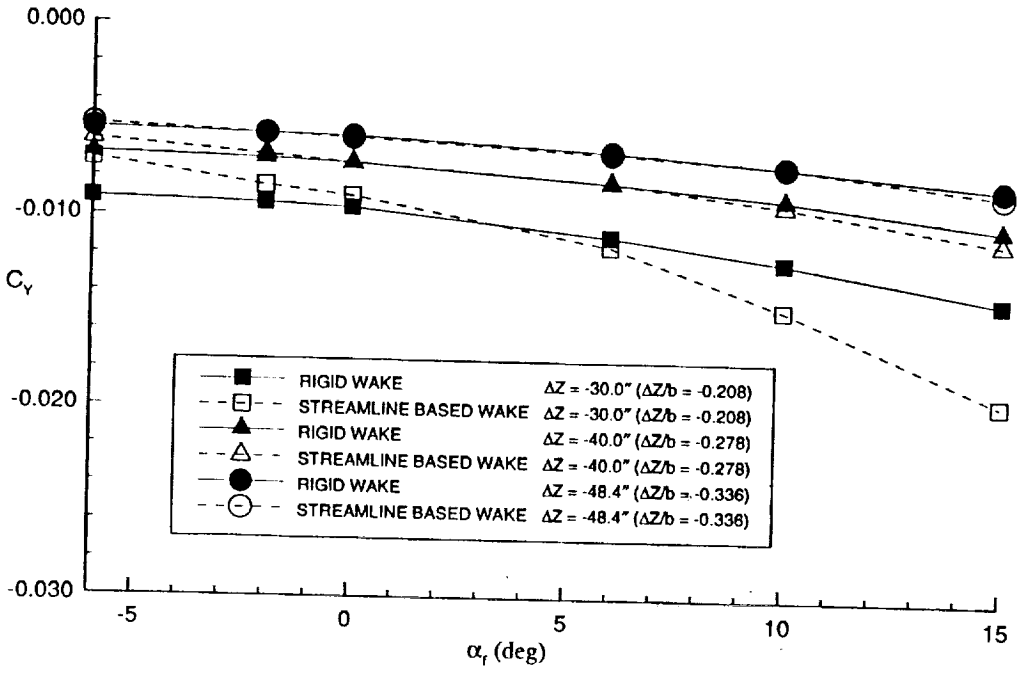

(b)

Figure 5.8 Effect of Streamline-Based Wake on Results
(a) Effect on C_l (b) Effect on C_Y

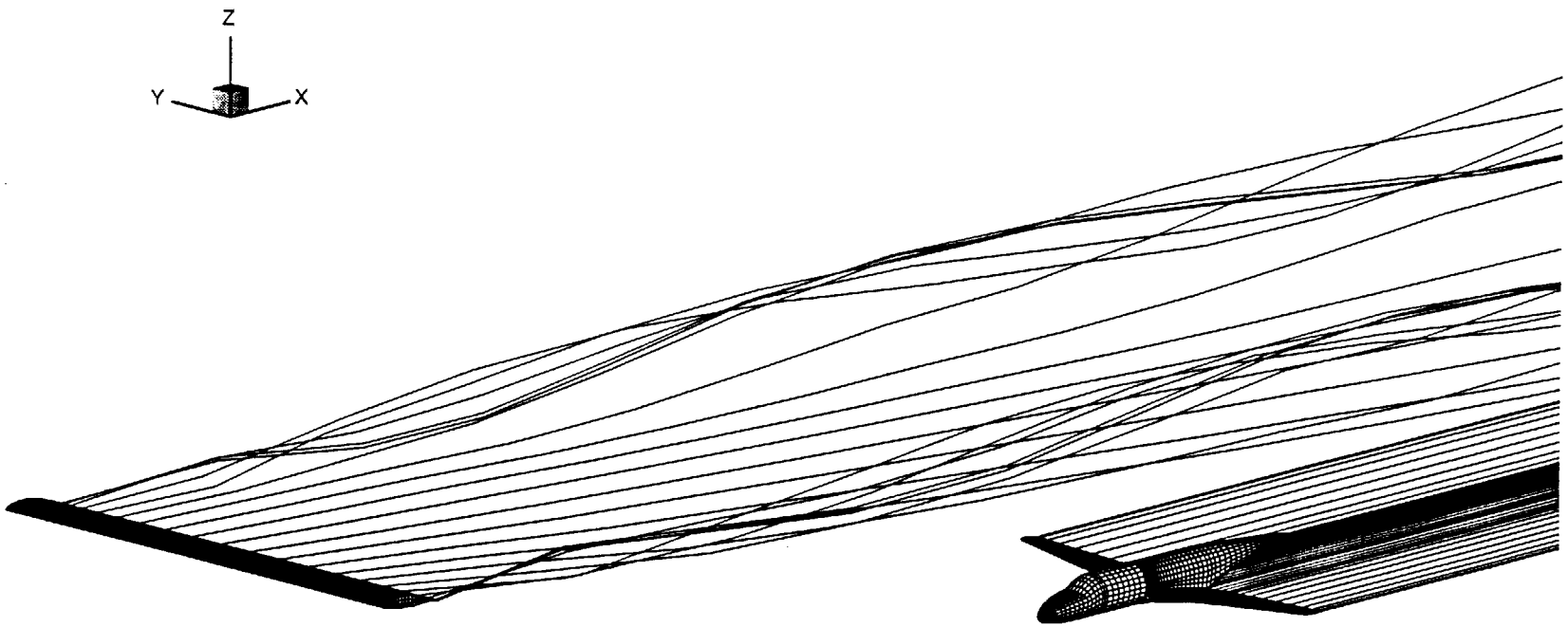

Figure 5.9 Wake-Vortex Interaction Between Generating Wing and Following Wing-Body Configuration Using Streamline-Based Wake on Generating Wing (DZ=-48.4 in., AZ/b = -0.139)

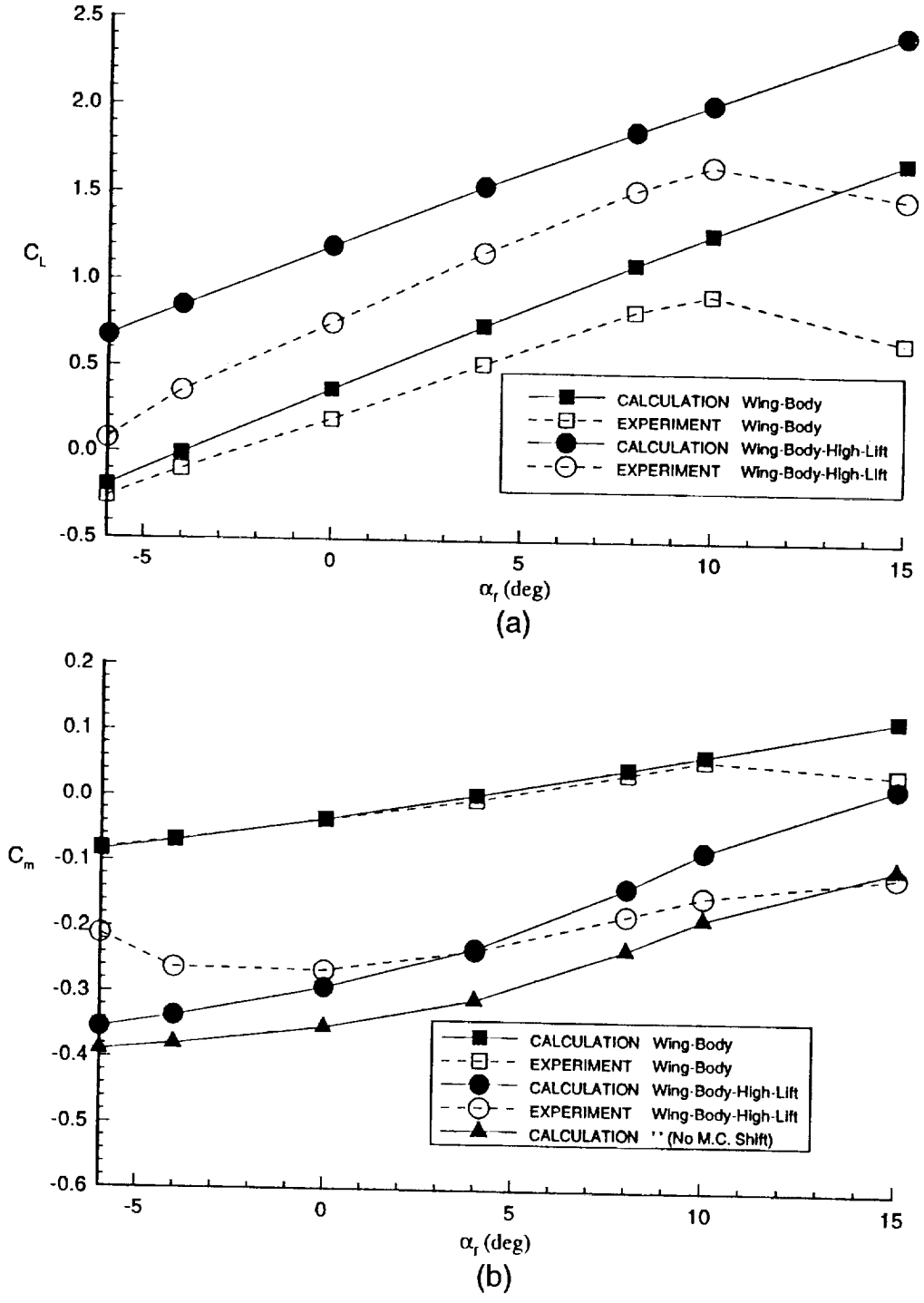

Figure 5.10 Effect of High-Lift System (No Vortex Case)
(a) Effect on C_L (b) Effect on C_m

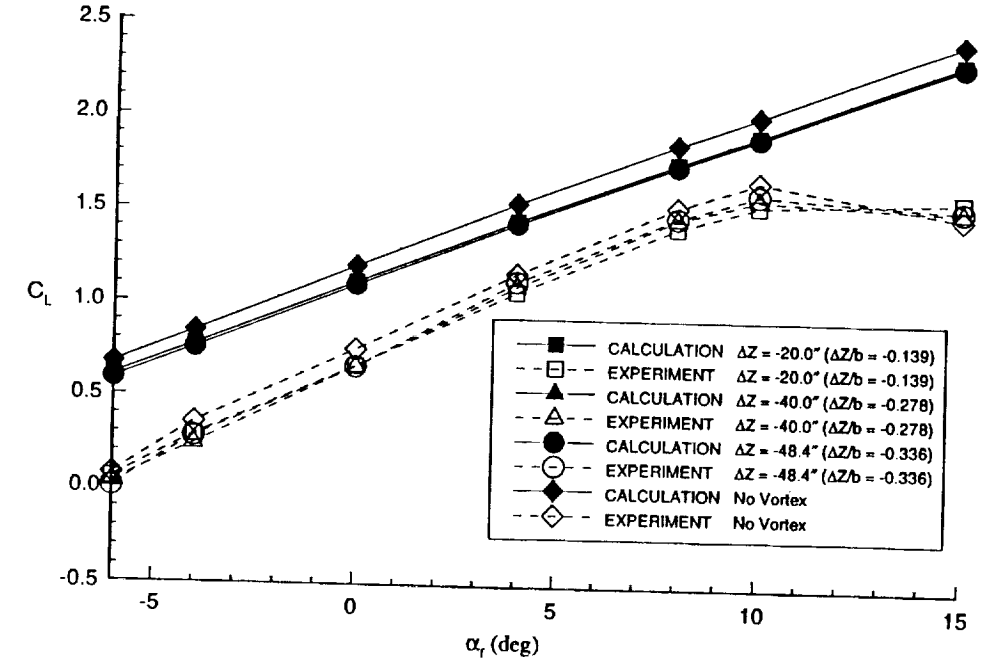

(a)

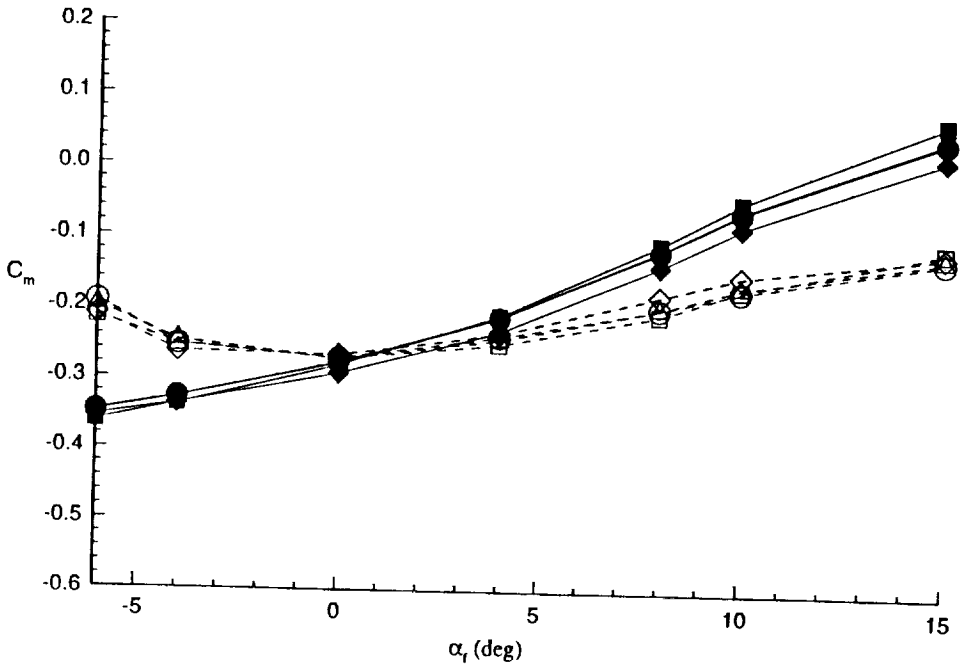

(b)

Figure 5.11 Comparison of Aerodynamic Characteristics for the Following Wing-Body Configuration with High-Lift System
(a) C_L Comparison (b) C_m Comparison

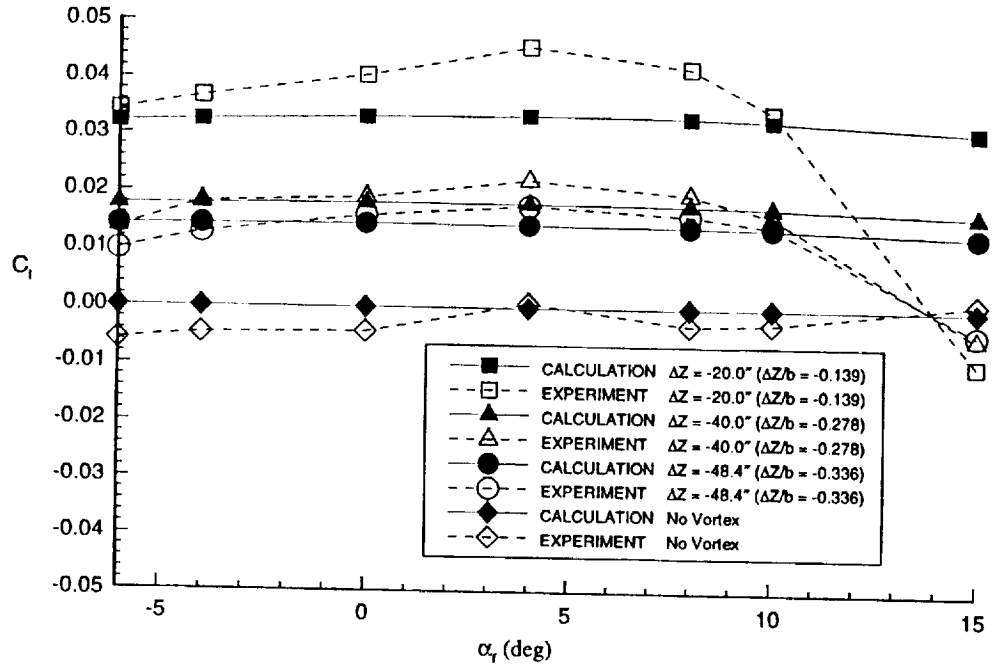

(c)

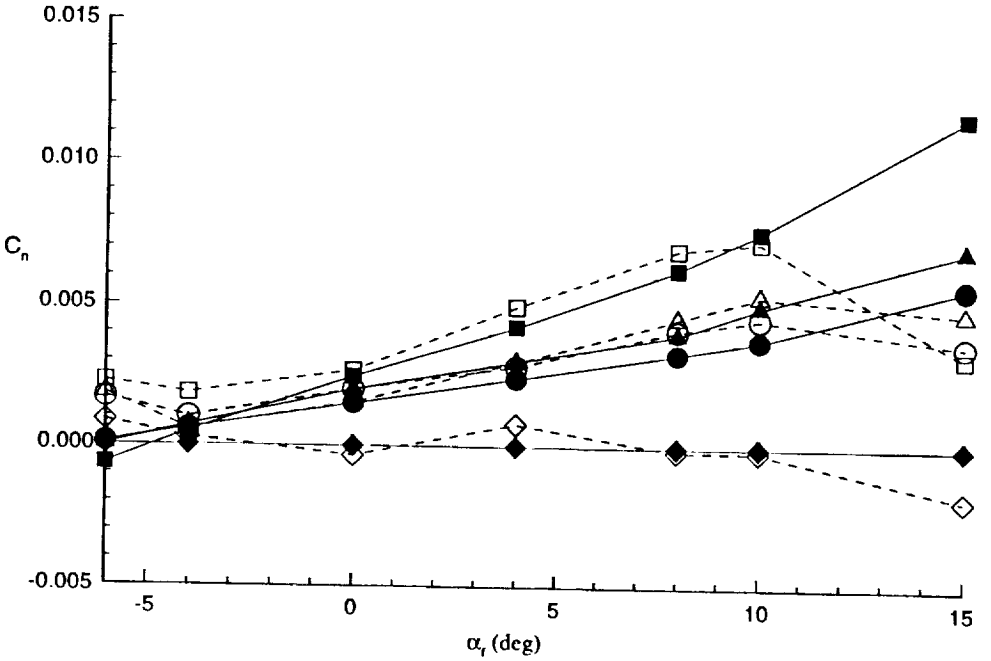

(d)

Figure 5.11 Comparison of Aerodynamic Characteristics for the Following Wing-Body Configuration with High-Lift System
(c) C_l Comparison (d) C_n Comparison

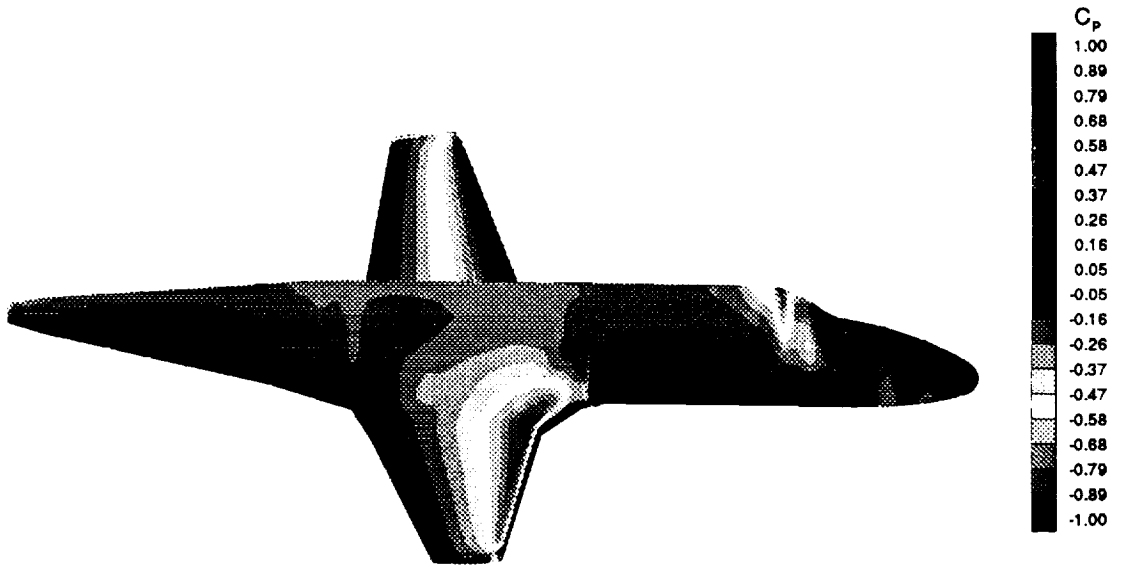

(a)

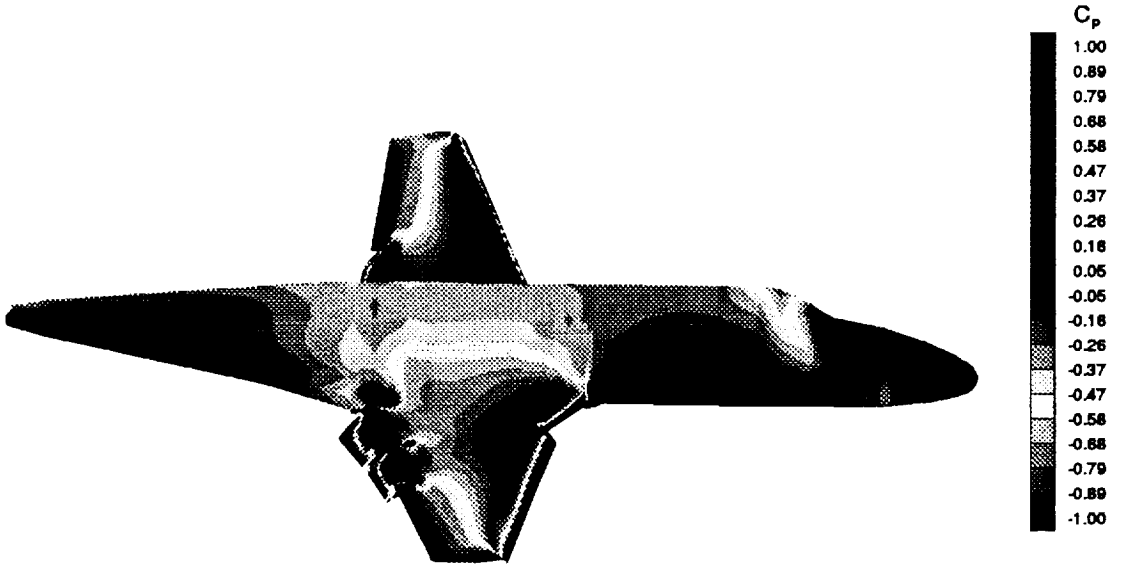

(b)

Figure 5.12 Pressure Contours for Wing-Body Configuration With and Without the High-Lift System (α_f = 0°, ΔZ = -20.0 in., $\Delta Z/b$ = -0.139)
(a) Without High-Lift System (b) With High-Lift System

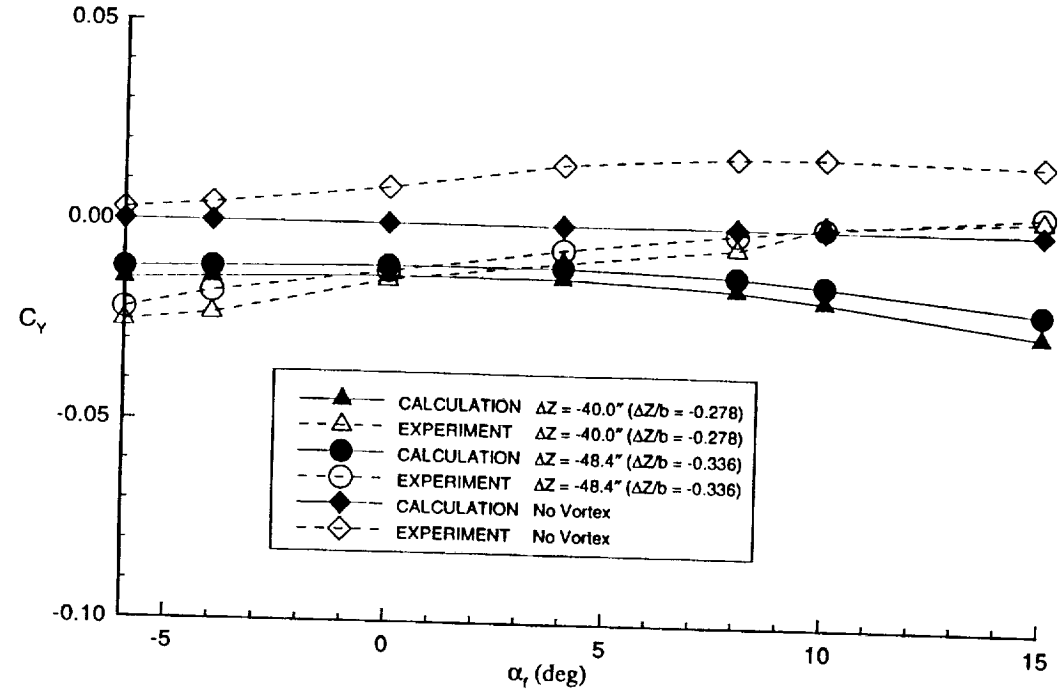

(a)

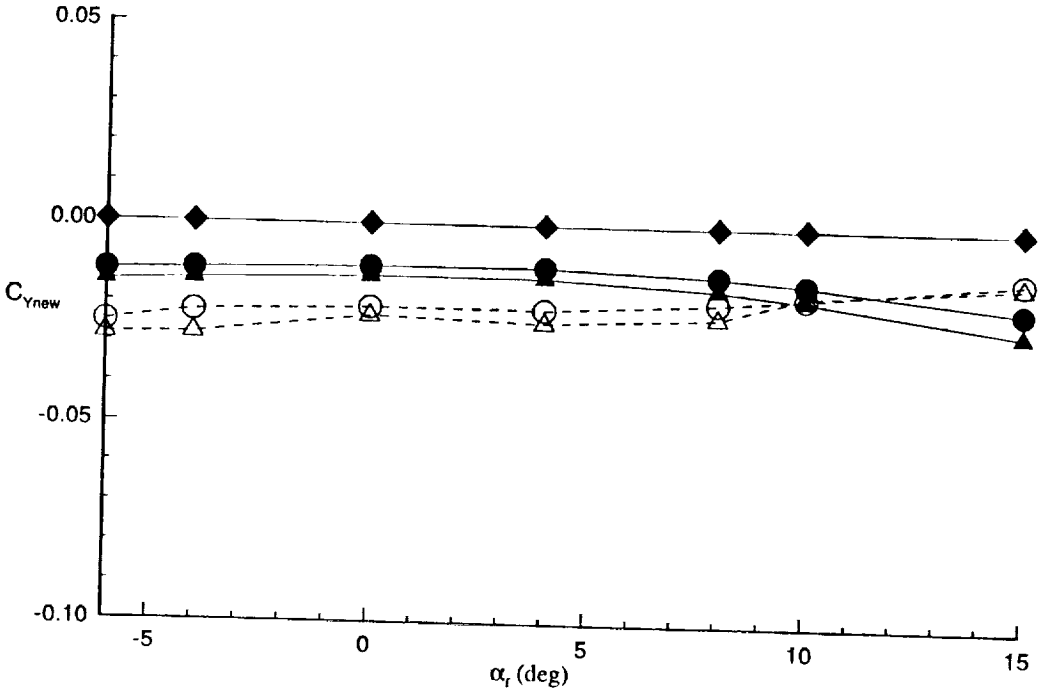

(b)

Figure 5.13 Side Force Comparison for the Following Wing-Body Configuration with High-Lift System (a) C_Y Comparison (b) New Unbiased C_Y

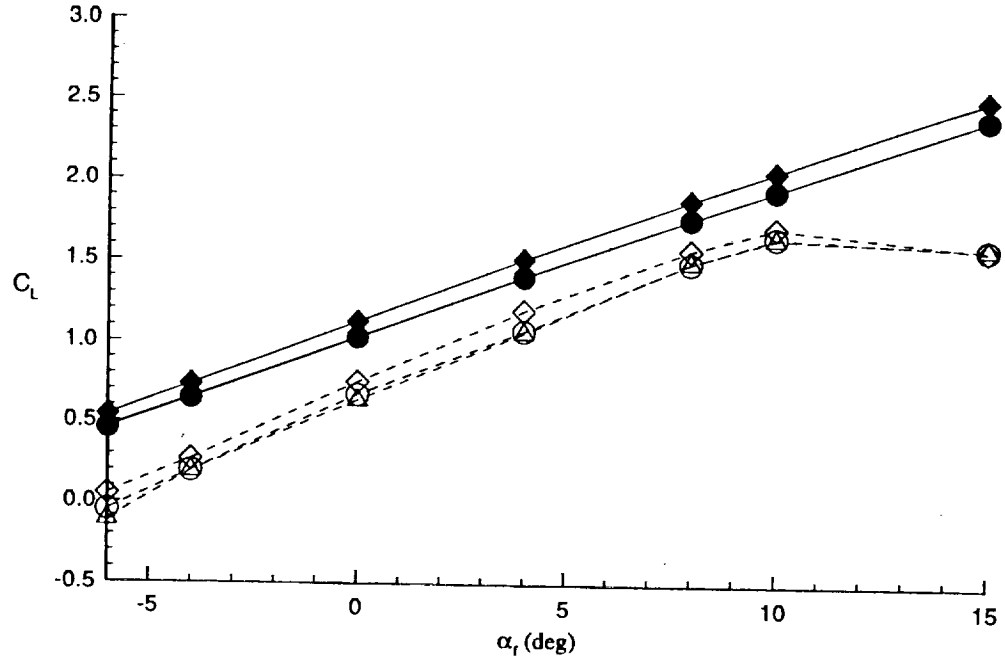

(a)

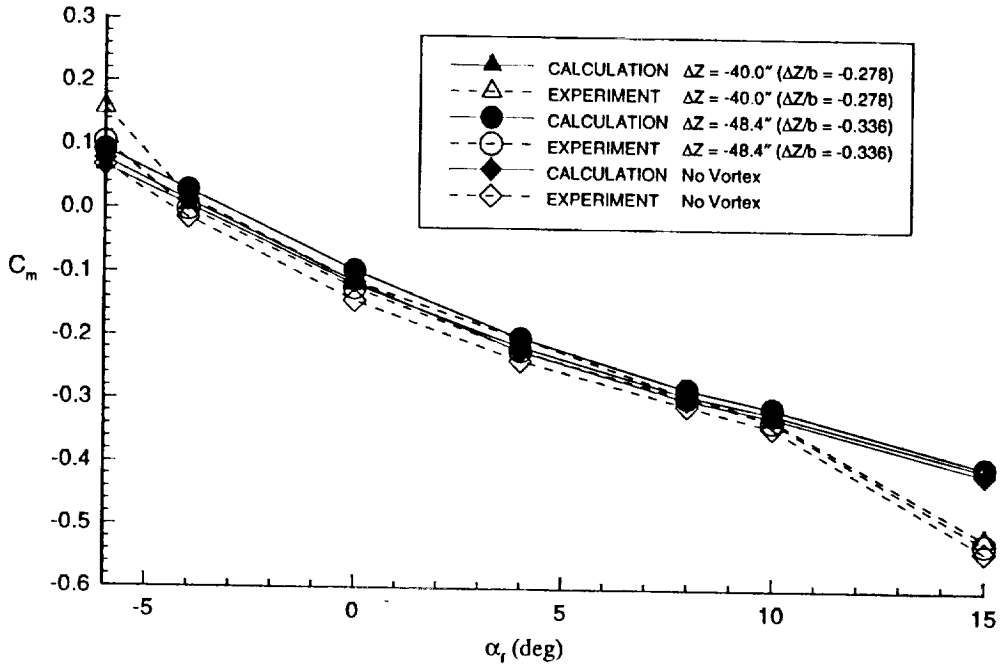

(b)

Figure 5.14 Comparison of Aerodynamic Characteristics for the Following Full- Computational Configuration (a) C_L Comparison (b) C_m Comparison

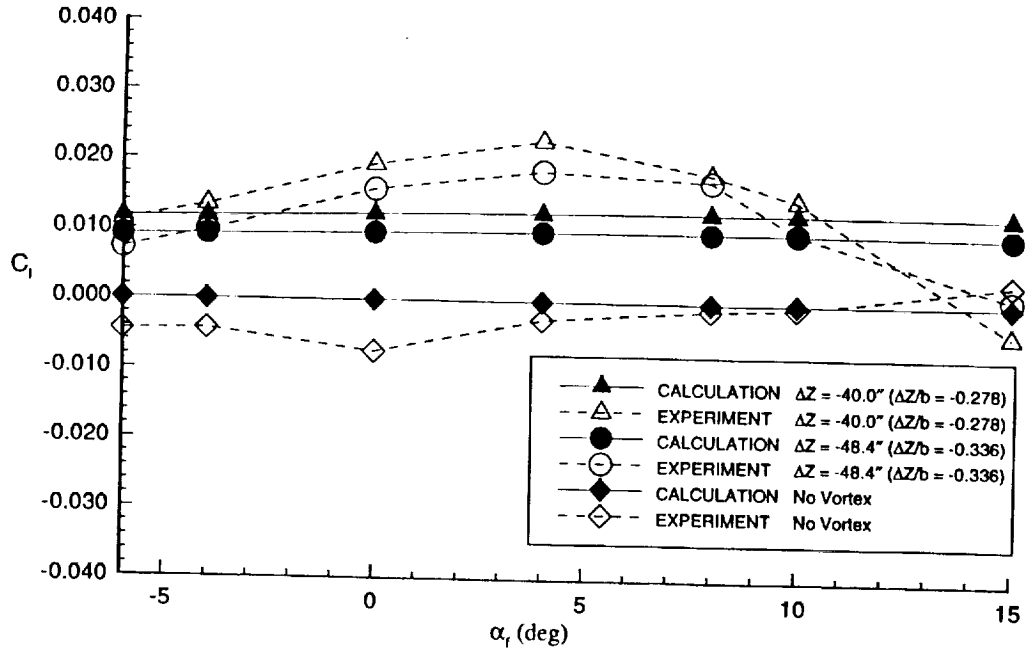

(c)

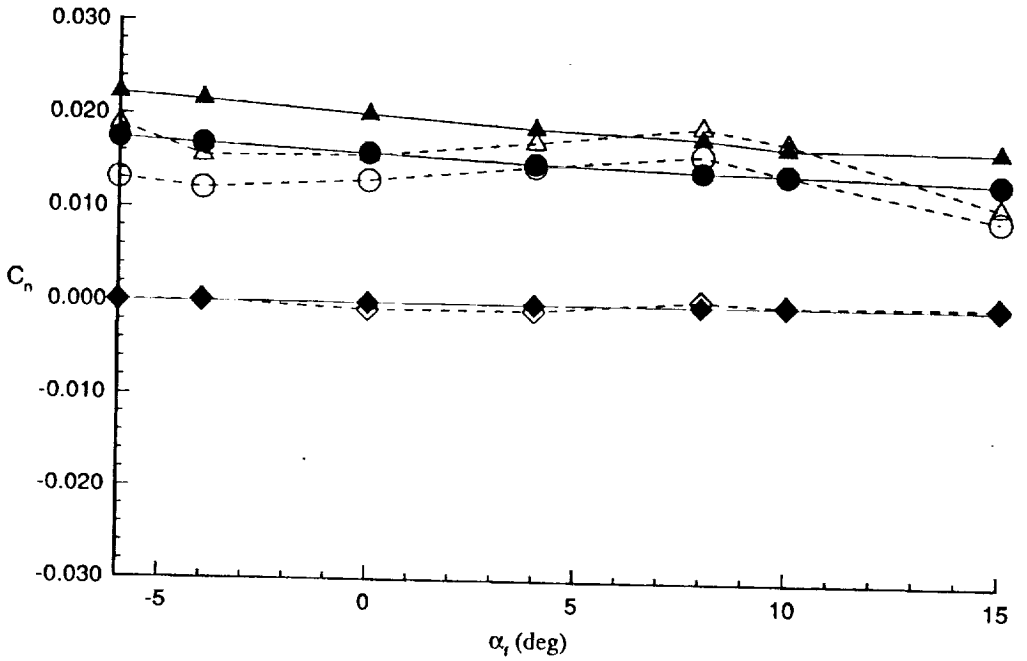

(d)

Figure 5.14 Comparison of Aerodynamic Characteristics for the Following Full- Computational Configuration (c) C_l Comparison (d) C_n Comparison

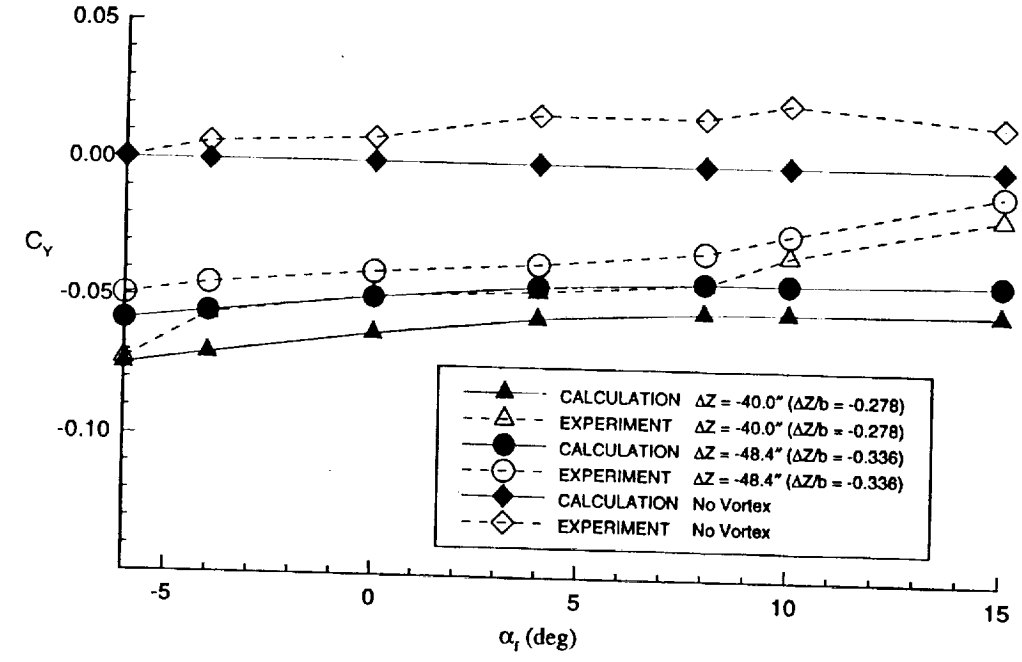

(e)

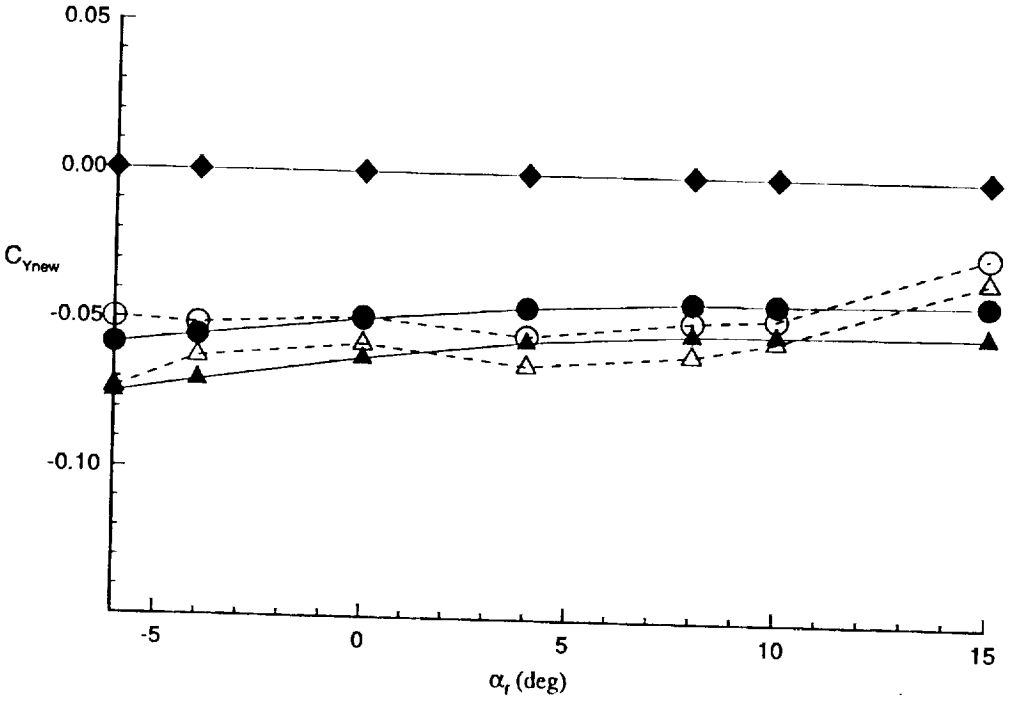

(f)

Figure 5.14 Comparison of Aerodynamic Characteristics for the Following Full- Computational Configuration (e) C_Y Comparison (f)New Unbiased C_Y

6.0 Conclusions and Recommendations

Understanding the wake-vortex/airplane interaction phenomenon is important to help define the parameters which can be used to predict a wake-vortex hazard . In an attempt to understand this phenomenon, efforts are underway utilizing various computational tools as a means of modeling and verifying wake-vortex hazard encounters. In this study, the capability of the 3-D, inviscid, incompressible code, PMARC, to model the interaction between the wake generated by a rectangular wing and a following business-jet model is assessed. Computational results are compared to wind-tunnel data. The effects of the different wake techniques used on the generating wing, modeling techniques, and the addition of the fuselage, high-lift system and the empennage on the following configuration are addressed. The primary conclusions of this study are:

- The investigation of various wake techniques demonstrates that the streamline-based wake technique is the more accurate technique to employ due to its ability to model wake roll-up and trajectory as well as its capacity to impose a realistic vortex velocity distribution on the following configuration.
- At negative vertical distances greater or equal to approximately 30% of the generating wing span from the vortex core, the steady-state, rigid wake utilized on the generating wing provided analogous results for the following configuration as the streamline-based wake.
- The code did not accurately predict the interaction effects of the vortex on the following model while near the ground (positive vertical distances).
- Results for the rolling-moment coefficient, C_l, obtained at negative vertical distances were well predicted for the interaction between the vortex and the wing-only model.

- The addition of the fuselage on the following configuration resulted in very good comparisons with wind-tunnel data for C_m, C_l, and C_n up to α_f of 8-10° where flow-separation effects become significant. Lift coefficient, C_L, was not well predicted by the inviscid method due to Reynolds number effects. Side-force coefficient, C_Y, was well predicted at distances greater or equal to approximately 30% of the span of the generating wing.
- The shift in the lift curve, ΔC_L, due to the addition of the high-lift system, is overpredicted by the inviscid code, PMARC. Flow separation in conjunction with differences between the actual and the modeled high-lift geometry causes discrepancies in the pitching-moment predictions. However, C_l and C_n are still well predicted.
- The addition of the tail further produces non-linearities due to the differences between the computational and experimental velocity flow fields surrounding the tail. Magnitudes and trends for C_m, C_l, C_n, and C_Y, however, are still well predicted.

The results of this study illustrate the code's capability in modeling the wake-vortex interaction problem. PMARC's ability to model complex configurations with only a surface grid as well as its ability to model wake roll-up make it a viable computational tool. Limitations, however, include the inability of the code to model viscous effects as well as its inability to model wake dissipation and decay. Furthermore, the following configuration is limited to distances at which the vortex lines of the generating wing do not penetrate the surface of the following configuration. This is a substantial limitation to the wake-vortex encounter study.

Future modifications of the code that would resolve the panel penetration problem include the introduction of an accurate velocity field onto the following configuration rather than a vortex wake or the integration of the

subvortex technique as defined by Maskew[46]. This technique involves the increase of panels in areas where vortex penetration occurs, allowing the vortex lines to deflect around the surface geometry. The former, however, would require a significant rewrite in the boundary conditions of the code, and the latter would require a large increase in CPU time. To further understand the code's capabilities, several issues have to be addressed for further study. Comparisons, for instance, need to be achieved for various locations of the following configuration to validate the code's ability to predict moments everywhere in the field. As mentioned earlier, another study would be the utilization of a streamline-based wake on the following configuration to account for the difference between computational and experimental velocity flow fields surrounding the tail. Improved comparisons can be further achieved through the use of viscous field codes. However, until 3-D viscous solutions are practical, the use of 3-D potential methods such as PMARC can be a useful tool in determining the wake-vortex encounter characteristics.

References

[1]Baart, D., Rovinsky, R.B., Monk, H. and Schweiker, M., "Effect of Reduced Intrail Separations on Capacity," Proceedings of the Aircraft Wake-Vortex Conference, Vol I, June 1992.

[2]Dunlay, W.J. and Muldoon, J.P., "Effect of Wake Vortex Interaction on Delays at Laguardia Airport, " Proceedings of the Aircraft Wake-Vortex Conference, Vol I, June 1992.

[3]Loney, M.R. and Goldberg, D.F., "The Benefits of Reduced Spacing Separation Standards at Chicago O' Hare International Airport," Proceedings of the Aircraft Wake-Vortex Conference, Vol I, June 1992.

[4]*Airman Information Manual - Official Guide to Basic Flight Information and ATC Procedures*. U.S. Department of Transportation, FAA, Paras 7-49, February 4, 1993.

[5]Burnham, D.C., "How to Use Wake Vortex Measurements To Set Separation Standards," Proceedings of the Aircraft Wake-Vortex Conference, Vol II, June 1992.

[6]Stough, H.P., Greene, G.C., Stewart, E.C., Stuever, R.A., Jordan, F.L., Rivers, R.A., and Vicroy, D.D., "NASA Wake-Vortex Research," AIAA Paper 93-4004, August 1993.

[7]Greene, G.C., Dunham, R.E., Burnham, D.C., Hallock, J.N., and Rossow, V. J., "Wake Vortex Research Lessons Learned," Proceedings of the Aircraft Wake-Vortex Conference, Vol I, June 1992.

[8]Rossow, V. J., "Prospects for Alleviation of Hazard Posed By Lift-Generated Wakes, " Proceedings of the Aircraft Wake-Vortex Conference, Vol I, June 1992.

[9]"Underwing Compression Vortex-Attenuation Device," NASA Tech Briefs, November 1994, pp. 86-88.

[10]Meyers, J. F., "Doppler Global Velocimetry The Next Generation?," AIAA Paper 92-3897.

[11]Branstetter, J.R., Hastings, E.C. and Patterson, J.C., "Flight Test to Determine Feasibility of a Proposed Airborne Wake Vortex Detection Concept," NASA TM - 102672, April 1991.

[12]Krasny, R., "Computation of vortex sheet roll-up in the Trefftz plane," *Journal of Fluid Mechanics*. Vol. 184, pp. 123-155, 1987.

[13]Moore, D.W., "A Numerical Study of the Roll-up of a Finite Vortex Sheet," *Journal of Fluid Mechanics*. Vol. 63, part 2, pp. 225-235, 1974.

[14]Butter, D.J. and Hancock, G.J., "A Numerical Method for Calculating the Trailing Vortex System behind a Swept Wing at Low Speed," *The Aeronautical Journal of the Royal Aeronautical Society*. Vol. 75, pp. 564-568, 1971.

[15]Yeh, D.T. and Plotkin, A., "Vortex Panel Calculation of Wake Rollup Behind a Large Aspect Ratio Wing," *AIAA Journal*. Vol. 24, No. 9, pp. 1417-1423, 1986.

[16]Ribeiro, R.S. and Kroo, I., "Vortex-in-Cell Analysis of Wing Wake Roll-Up," AIAA Paper 92-2703 CP, 1992.

[17]Hoeijmakers, H.W.M., "Modeling and Numerical Simulation of Vortex Flow in Aerodynamics," NLR TP 91154 U, 1990.

[18]Kandil, O.A., Wong, Tin-Chee, and Liu, Chen-Huei, "Turbulent Flow Over A 747/747 Generator/Follower Configuration and Its Dynamic Response," AIAA Paper 94-2383, June 1994.

[19]Behr, R. and Wagner, S., " A Vortex-Lattice Method For the Calculation of Vortex Sheet Roll-Up and Wing-Vortex Interaction," *Finite Approximation and Fluid Mechanics II; DFG Priority Research Program Results, 1986-1988, Notes on Numerical Fluid Mechanics Series*, Vol. 25, 1989, pp. 1-14.

[20]Bloy, A.W. and West, M.G., "Interference between Tanker Wing Wake with Roll-Up and Receiver Aircraft," paper submitted for publication in Journal of Aircraft, June 1993.

[21]Rossow, V.J., "Wake-Vortex Structure from Lift and Torque Induced on a Following Wing," AIAA Paper 93-3013, July 1993.

[22]Stewart, E.C., "A Study of the Interaction Between A Wake Vortex and an Encountering Airplane," AIAA Paper 93-3642, August 1993.

[23]Smith, B.E. and Ross, J.C., "Application of a Panel Method to Wake-Vortex/Wing Interaction and Comparison with Experimental Data," NASA TM-88337, September 1987.

[24]Maskew, B. and Rao, B.M., "VSAERO User's Manual, ", October 1983.

[25]Hoeijmakers, H.W.M., " Panel Methods in Aerodynamics; Some Highlights," NLR MP 87028 U, 1987.

[26]Maskew, B., "Prediction of Subsonic Aerodynamic Characteristics - A Case for Low-Order Panel Methods," AIAA Paper 81-0252, January 1981.

[27]Ashby, D.L., Dudley, M.R., Iguchi, S.K., Browne, L., Katz, J., "Potential Flow Theory and Operation Guide for the Panel Code Pmarc_12," NASA TM-102581, January 1991.

[28]Ashby, D.L., Dudley, M.R., Iguchi, S.K., "Development and Validation of an Advanced Low-Order Panel Method," NASA TM-101024, October 1988.

[29]Hoeijmakers, H.W.M., "Aerodynamics of Vortical Type Flows in Three Dimensions," AGARD CP-342, pp. 18-1 through 18-18, 18-27.

[30]Labrujere, Th.E. and de Vries, O., "Evaluation of a Potential Theoretical Model of the Wake Behind A Wing Via Comparison of Measurements and Calculations," NLR TR 74063U, 1974.

[31]Barnwell, R.W. and Hussaini, M.Y., *Natural Laminar Flow and Laminar Flow Control*, ICASE/NASA LaRC Series, Springer-Verlag Inc., New York, 1992.

[32]Coe, P. L., Turner, S. G., and Owens, D. B., "Low-Speed Wind-Tunnel Investigation of the Flight Dynamic Characteristics of an Advanced Turboprop Business/Commuter Aircraft Configuration," NASA Technical Paper 2982, 1990, pp. 13-19.

[33]Somers, D. M., "Design and Experimental Results for a Flapped Natural-Laminar-Flow Airfoil for General Aviation Applications," NASA TP 1865, June 1981.

[34]Katz, J. and Plotkin, A., *Low-Speed Aerodynamics, From Wing Theory to Panel Methods*, McGraw-Hill, Inc. New York, 1991, p. 370.

[35]Rae, W.H., Jr. and Pope, A., *Low-Speed Wind Tunnel Testing*, John Wiley & Sons, New York, 1984, p. 240.

[36]Dunham, D. M., Gentry, G.L., Manuel, G.S., Applin, Z.T. and Quinto, P.F., "Low-Speed Aerodynamic Characteristics of a Twin-Engine General Aviation Configuration With Aft-Fuselage-Mounted Pusher Propellers," NASA TP 2763, October 1987.

[37]Riegels, F. W., *Aerofoil Sections, Results from Wind-Tunnel Investigations Theoretical Foundations*, London, 1961, pp. 127-128.

[38]Jones, R.T., "Correction of the Lifting-Line Theory for the Effect of the Chord," NASA TN 817, July 1941.

[39]Abbott, I.H. and Von Doenhoff, A. E., *Theory of Wing Sections*, New York: 1959, p. 126.

[40]Baron, A. and Boffadossi, M., "Wake Structure and Aerodynamic Behavior of High Lift Aircraft Configurations During Unsteady Maneuvers in Ground Effect," AGARD-CP-515, October 1992, pp. 25-1 through 25-15.

[41]Rossow, V. J., "Effect of Ground and Ceiling Planes on Shape of Energized Wakes," AIAA-93-3410, August 1993.

[42]Zheng, Z. and Ash, R.L., "Viscous Effects on a Vortex Wake in Ground Effect," NASA-CR-190400, May 1991.

[43]Bilanin, A.J., Teske, M.E., and Hirsh, J.E., "Neutral Atmospheric Effects on the Dissipation of Aircraft Vortex Wakes," AIAA Journal, Vol. 16, No. 9, 1978, pp. 956-961.

[44]Smith, H., *The Illustrated Guide to Aerodynamics*, Tab Books, 1985, pp. 62-64.

[45]Lan, C. E. and Roskam, J., *Airplane Aerodynamics and Performance*, The University of Kansas, 1980, p. 80.

[46]Maskew, B., "A Subvortex Technique for the Close Approach to a Discretized Vortex Sheet," NASA TM 2487, September 1975.

[47]Gainer, T. G. and Hoffman, S., "Summary of Transformation Equations and Equations of Motion Used in Free-Flight and Wind-Tunnel Data Reduction and Analysis," NASA SP-3070, 1972.

Appendix A : Potential-Flow Theory Behind PMARC

PMARC is an incompressible, inviscid, irrotational flow code based on potential theory. The condition of irrotational flow produces an exact differential of a velocity potential, $\Phi(x,y,z)$, which is defined as

$$\vec{V} = \nabla\Phi \tag{A.1}$$

where $\vec{V} = u\vec{i} + v\vec{j} + w\vec{k}$

Substitution into the continuity equation yields,

$$\frac{\partial\rho}{\partial t} + \frac{\partial}{\partial x}\left(\rho\frac{\partial\Phi}{\partial x}\right) + \frac{\partial}{\partial y}\left(\rho\frac{\partial\Phi}{\partial y}\right) + \frac{\partial}{\partial z}\left(\rho\frac{\partial\Phi}{\partial z}\right) = 0 \tag{A.2}$$

In the case of steady, incompressible flow, $\partial/\partial t$=0 and ρ = constant, Laplace's equation is obtained:

$$\nabla^2\Phi = 0 \tag{A.3}$$

Figure A.1 depicts the model nomenclature used to define a configuration in the potential flow field. In this model, both the external potential, (Φ), and internal potential, (Φ_i), are assumed to satisfy equation (A.3), such that

$$\nabla^2\Phi = 0 \quad and \quad \nabla^2\Phi_i = 0$$

Application of Green's theorem to Laplace's equation results in a solution that can be constructed by the sum of source (σ) and doublet (μ) strengths distributed along the surface boundary S_b. The potential anywhere in the flow field can be described by:

$$\Phi(x,y,z) = -\frac{1}{4\pi}\iint_{S_b}\left[\sigma\left(\frac{1}{\vec{r}}\right) - \mu\vec{n}\cdot\nabla\left(\frac{1}{\vec{r}}\right)\right]dS + \Phi_\infty \tag{A.4}$$

where the freestream potential, Φ_∞, is defined as

$$\Phi_\infty = u_\infty x + v_\infty y + w_\infty z$$

Modeling the wake as thin doublet or vortex sheets, Equation (A.4) can be re-written as:

$$\Phi(x,y,z) = \frac{1}{4\pi}\iint_{S_b+S_w}\mu\vec{n}\cdot\nabla\left(\frac{1}{\vec{r}}\right)dS - \frac{1}{4\pi}\iint_{S_b}\sigma\left(\frac{1}{\vec{r}}\right)dS + \Phi_\infty \tag{A.5}$$

Implementation of a Dirichlet boundary condition to the internal potential reduces Equation (A.5) to a simpler form. This boundary condition sets the internal potential equal to the freestream potential,

$$\Phi_i = \Phi_\infty \tag{A.6}$$

resulting in a perturbation potential, φ, of

$$\varphi = \Phi_i - \Phi_\infty = 0 \tag{A.7}$$

Rewriting the forms of the doublet and source terms and applying the Dirichlet boundary condition results in the new form of the above equation:

$$\frac{1}{4\pi}\iint_{S_b+S_w} \mu \frac{\partial}{\partial n}\left(\frac{1}{\bar{r}}\right) dS - \frac{1}{4\pi}\iint_{S_b} \sigma\left(\frac{1}{\bar{r}}\right) dS = 0 \tag{A.8}$$

From the application of the Neumann boundary condition, $\partial\Phi/\partial n = 0$, on the surface S_b to equation (A.4), we obtain:

$$\sigma = \vec{n} \cdot \vec{V}_\infty \tag{A.9}$$

Equation (A.8) can be rewritten in discretized form, breaking the integral up into surface integrals over each panel. Factoring out the constant doublet and source strengths and taking a point on a panel to be inside the surface of the panel at its centroid results in a new discretized equation:

$$\sum_{k=1}^{N_s}(\mu_k C_k) + \sum_{k=1}^{N_s}(\sigma_k B_k) + \sum_{k=1}^{N_w}(\mu_k C_k) = 0 \tag{A.10}$$

where N_S represents the number of surface panels and N_w represents the number of wake panels. The coefficients B_k and C_k represent the velocity potential influence coefficients per unit strength and are functions of geometry, such that,

$$\begin{aligned} B_k &= -\frac{1}{4\pi}\iint_k \frac{1}{\bar{r}} dS_k \\ C_k &= \frac{1}{4\pi}\iint_k \frac{\partial}{\partial \bar{n}}\left(\frac{1}{\bar{r}}\right) dS_k \end{aligned} \tag{A.11}$$

Equation (A.10) can be reduced to the following linear system:

$$[A][\mu]=[D] \tag{A.12}$$

where $[\mu]$ is the only unknown. [D] is known because the source strengths are known as a result of Equation (A.9). Once the doublet strengths are determined, the perturbation potential and therefore the velocity components are obtained. From the resultant velocity at each control point, the pressure coefficients can subsequently be obtained through the equation:

$$C_{p_k}=1-\frac{V_k^{\,2}}{V_\infty^{\,2}} \tag{A.13}$$

For a more extensive formulation, see reference 27 and reference 34.

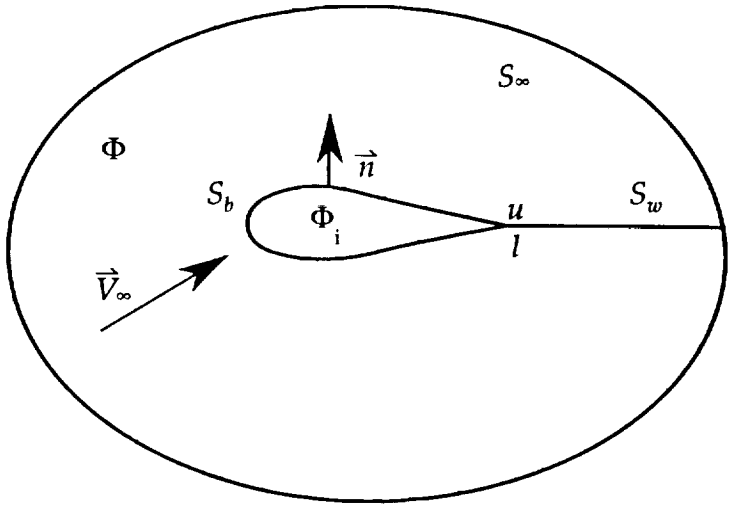

Figure A.1 Description of the Potential-Flow Model

Appendix B : Axes-System Conversion

To accurately correlate the experimental results with the computational results it was necessary to convert PMARC's calculated moment coefficients imparted in the wind-axes system to the body-axes system. Figure B.2 depicts both coordinate systems. Notice that PMARC defines the x and z axes of the wind-coordinate system as the negative of the standard definition of the wind-axes system. This is because PMARC's definition of the wind-coordinate system relates to the axes definition of the constructed geometric model. The transformation equations from wind to body axes are taken from Gainer and Hoffman[47] and can easily be attained from Figure B.1. The PMARC code, however, also non-dimensionalizes both the rolling moment and the yawing moment by the semi-span of the configuration. Therefore, in addition to the transformation, these particular moments had to be divided by two. The resulting equations are:

$$
\begin{aligned}
C_{Y_{body}} &= C_{Y_{wind}} \\
C_{m_{body}} &= C_{m_{wind}} \\
C_{l_{body}} &= -0.5 \times \left(C_{l_{wind}} \times \cos(\alpha) - C_{n_{wind}} \times \sin(\alpha) \right) \\
C_{n_{body}} &= -0.5 \times \left(C_{n_{wind}} \times \cos(\alpha) + C_{l_{wind}} \times \sin(\alpha) \right)
\end{aligned}
\qquad \text{(B.1)}
$$

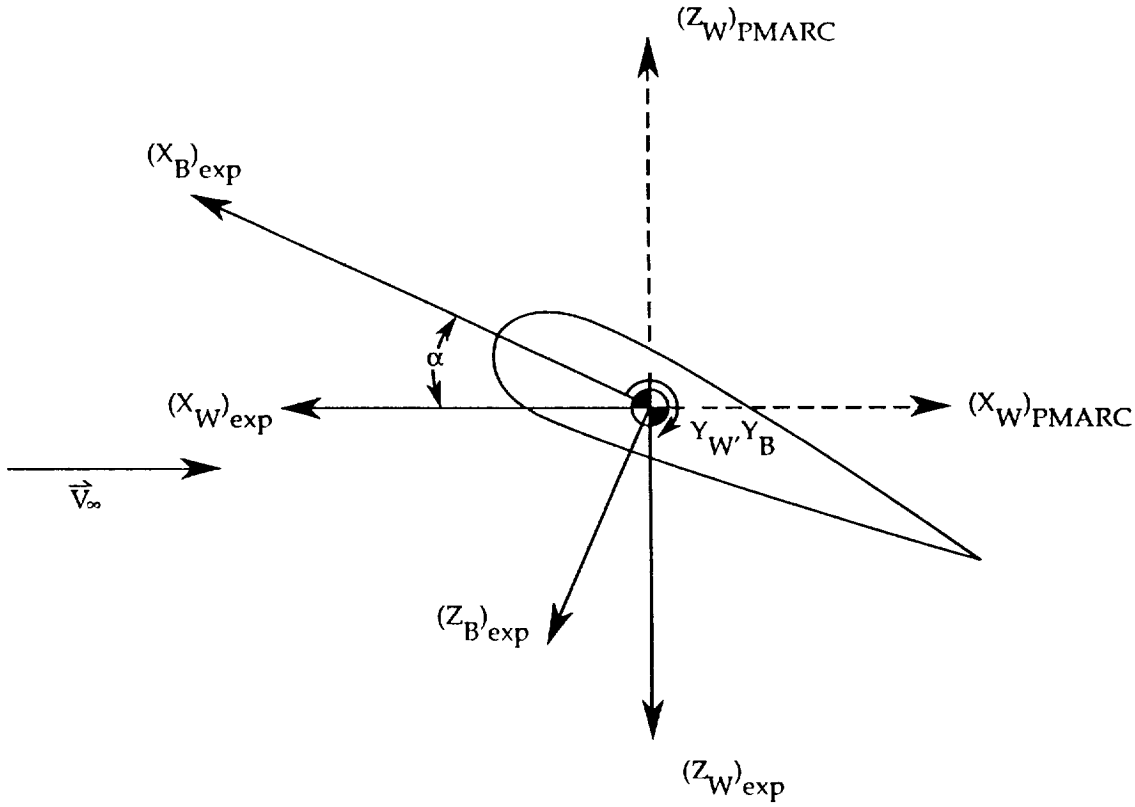

Figure B.2 Axes System for PMARC and the Wind-Tunnel Experiment